








## RESEARCH ARTICLE

10.1029/2022GC010393

## High-Pressure and High-Temperature Single-Crystal Elasticity of Cr-Pyropite: Implications for the Density and Seismic Velocity of Subcontinental Lithospheric Mantle

Jingui Xu<sup>1,2</sup> , Dawei Fan<sup>1</sup> , Bo Li<sup>3</sup>, Sergey N. Tkachev<sup>4</sup> , Vitali B. Prakapenka<sup>4</sup> , Dongzhou Zhang<sup>2</sup> , Guangzhong Yang<sup>5</sup>, Yi Zhou<sup>6</sup>, and Wenge Zhou<sup>1</sup>

<sup>1</sup>Key Laboratory for High-Temperature and High-Pressure Study of the Earth's Interior, Institute of Geochemistry, Chinese Academy of Sciences, Guiyang, China, <sup>2</sup>Hawai'i Institute of Geophysics and Planetology, School of Ocean and Earth Science and Technology, University of Hawai'i at Manoa, Honolulu, HI, USA, <sup>3</sup>Research Institute of Petroleum Exploration & Development-Northwest (NWGI), PetroChina, Lanzhou, China, <sup>4</sup>Center for Advanced Radiation Sources, University of Chicago, Chicago, IL, USA, <sup>5</sup>The No. 101 Geological Brigade, Geological and Mineral Exploration and Development Bureau of Guizhou Province, Kaili, China, <sup>6</sup>School of Geoscience and Technology, Southwest Petroleum University, Chengdu, China

## Key Points:

- Single-crystal elastic properties of Cr-pyropite of the subcontinental lithospheric mantle are measured at high pressure and high temperature
- The results are used to model the density and velocity of three typical types of subcontinental lithospheric mantle
- The compositional effects are notable on the density but insignificant on the velocity of the subcontinental lithospheric mantle

## Supporting Information:

Supporting Information may be found in the online version of this article.

## Correspondence to:

D. Fan,  
fandawei@vip.gyig.ac.cn

## Citation:

Xu, J., Fan, D., Li, B., Tkachev, S. N., Prakapenka, V. B., Zhang, D., et al. (2022). High-pressure and high-temperature single-crystal elasticity of Cr-pyropite: Implications for the density and seismic velocity of subcontinental lithospheric mantle. *Geochemistry, Geophysics, Geosystems*, 23, e2022GC010393. <https://doi.org/10.1029/2022GC010393>

Received 18 FEB 2022

Accepted 14 JUL 2022

**Abstract** Single-crystal X-ray diffraction and Brillouin spectroscopy experiments were performed on a natural Cr-pyropite ( $\text{Prp}_{71.0}\text{Alm}_{12.6}\text{Sps}_{0.7}\text{Gr}_{3.5}\text{Uvr}_{12.2}$ ) at high pressure and high temperature up to 11.0 GPa and 800 K. Fitting the collected data to the third-order finite strain equation yields bulk modulus ( $K_{50}$ ), shear modulus ( $G_0$ ), their pressure ( $(\partial K_s/\partial P)_T$  and  $(\partial G/\partial P)_T$ ) and temperature ( $(\partial K_s/\partial T)_P$  and  $(\partial G/\partial T)_P$ ) derivatives,  $K_{50} = 167.7(8)$  GPa,  $G_0 = 91.5(5)$  GPa,  $(\partial K_s/\partial P)_T = 4.3(1)$ ,  $(\partial G/\partial P)_T = 1.4(1)$ ,  $(\partial K_s/\partial T)_P = -0.0175(1)$  GPa/K and  $(\partial G/\partial T)_P = -0.0073(1)$  GPa/K. Using the obtained results, we examined whether the elastic properties of the Cr-pyropite can be accurately calculated from those of endmembers including pyropite, almandine, grossular, and uvarovite assuming a linear relationship between elastic properties and composition (end-member model). The results indicate that the end-member model provides a sufficient approximation for the elastic properties of Cr-pyropite in calculating the density and velocity of the subcontinental lithospheric mantle (SCLM). We modeled the densities and velocities of three typical types of SCLM (Archon, Proton, and Tecton) in order to investigate how the variation of chemical composition influences the SCLM. We obtained that the compositional change from the Archon to the Tecton increases the density of the SCLM significantly, which can be an important prerequisite for SCLM delamination. However, the compositional variation only slightly changes the velocity of the SCLM and the change is within the uncertainty of the calculation. Moreover, in comparison to the velocity,  $\rho/V_p$  and  $\rho/V_s$  are much more sensitive to the compositional change of the SCLM.

**Plain Language Summary** Cr-pyropite is a major mineral of the subcontinental lithospheric mantle (SCLM). Determination of its thermoelastic parameters is thus important for modeling the density and seismic velocity of the SCLM. Due to the complex composition of SCLM Cr-pyropite in the evolution of the SCLM, it is necessary to examine whether the elastic properties of SCLM Cr-pyropite can be accurately calculated from those of end-member garnets. Here, we measured the single-crystal elastic properties of a natural Cr-pyropite at high pressure and high temperature. The results suggest that the elastic properties of Cr-pyropite at high pressure-temperature conditions in the SCLM can be reasonably calculated using the elastic parameters of the component end-member garnets. In combination with literature results, we investigated how the variation of chemical composition influences the density and seismic velocity of the SCLM. The results show that the compositional variation significantly influences the density of the SCLM, which can be an important factor in controlling the stability of the SCLM. By contrast, the compositional variation does not significantly influence the seismic velocity of the SCLM, and the effect is very limited in comparison to the effect of temperature variation.

### 1. Introduction

The subcontinental lithospheric mantle (SCLM) is the uppermost rigid part of the Earth's mantle overlain by the Earth's continental crust. Studies on xenoliths, xenocrysts, and mineral inclusions in igneous rocks suggest that garnet-peridotite is the representative rock of the SCLM (Griffin et al., 2009). Natural garnet commonly has complex composition, which is generally described as a solid solution of end members. The general formula of

© 2022 The Authors.

This is an open access article under the terms of the [Creative Commons Attribution-NonCommercial License](https://creativecommons.org/licenses/by-nc/4.0/), which permits use, distribution and reproduction in any medium, provided the original work is properly cited and is not used for commercial purposes.

silicate garnet is  $X_3Y_2Si_3O_{12}$ , and its common end members include pyrope ( $Prp_{100}$ ;  $Mg_3Al_2Si_3O_{12}$ ), almandine ( $Alm_{100}$ ;  $Fe_3Al_2Si_3O_{12}$ ), grossular ( $Grs_{100}$ ;  $Ca_3Al_2Si_3O_{12}$ ), spessartine ( $Sps_{100}$ ;  $Mn_3Al_2Si_3O_{12}$ ), uvarovite ( $Uvr_{100}$ ;  $Ca_3Cr_2Si_3O_{12}$ ), knorringite ( $Knr$ ;  $Mg_3Cr_2Si_3O_{12}$ ), and andradite ( $Adr_{100}$ ;  $Ca_3Fe_2^{3+}Si_3O_{12}$ ). However, garnet in SCLM peridotite is characterized by its high  $Cr_2O_3$  content (Griffin et al., 1999). The chemical properties of SCLM have been established based on mantle xenoliths and xenocrysts brought by igneous rocks to the surface (e.g., Griffin et al., 2003). The volumes of SCLM are classified based on the tectonothermal age of the overlying crust into Archons ( $\geq 2.5$  Ga), Protons (2.5–1.0 Ga), and Tectons ( $< 1.0$  Ga; Griffin et al., 2009). Although the silicate Earth contains  $Cr_2O_3$  less than 0.5 wt.%, the  $Cr_2O_3$  content in SCLM Cr-pyrope is much higher, as shown in Griffin et al. (1999), the statistics for Cr-pyrope show that the median  $Cr_2O_3$  contents are 5.3, 4.1, and 2.0 wt. % for the Archon, Proton and Tecton Cr-pyrope, respectively. Fluid/melt metasomatism in the SCLM was proposed to be an important cause to form Cr-pyrope (Malkovets et al., 2007), and has been identified in peridotitic xenoliths from various cratons (e.g., Agashev et al., 2013; Shchukina et al., 2015; Shu & Brey, 2015). Therefore, the elastic properties of Cr-pyrope are necessary to interpret the seismic data of the SCLM obtained by seismology and further model the seismic velocity.

To date, many experimental studies have reported the elastic properties of pyrope since Leitner et al. (1980) and O'Neill et al. (1991) measured the single-crystal elasticity of  $Prp_{100}$  at ambient conditions by the Brillouin light scattering (BLS) method. With the development of high-pressure ( $P$ ) techniques, the high- $P$  elasticity of pyrope was studied by BLS (Fan et al., 2019; Sinogeikin & Bass, 2000) and ultrasonic interferometry (UI; Chantel et al., 2016; Chen et al., 1999; Gwanmesia et al., 2006; Zou, Irifune, et al., 2012) methods. Meanwhile, several studies reported the elasticity of pyrope and Fe-rich pyrope at high  $P$  and high temperature ( $T$ ) (Chantel et al., 2016; Fan et al., 2019; Gwanmesia et al., 2007; Lu et al., 2013; Zou, Irifune, et al., 2012). By comparison, elastic property studies on Cr-pyrope are very limited (Babuška et al., 1978; Suzuki & Anderson, 1983). Babuška et al. (1978) measured the elastic properties of four Cr-pyropes ( $Cr\# = 5-9$ ;  $Cr\# = Cr/(Cr + Al)$ ) by means of the rectangular parallelepiped resonance (RPR) method at room  $P$ - $T$ . Using the same method, Suzuki and Anderson (1983) investigated the high- $T$  elasticity of a natural Cr-pyrope ( $Cr\# = 6$ ) to 1000 K at room  $P$ . To the best of our knowledge, there is still no elastic property study of Cr-pyrope at high  $P$  and high  $T$ .

The elastic properties of solid solution composition are often thought to be calculated from the end-member elastic properties assuming a linear dependence of the elastic properties with composition (e.g., Ita & Stixrude, 1992; O'Neill et al., 1989). Two kinds of cation substitution can occur at the  $X$ - (dodecahedral coordination) and  $Y$ -site (octahedral coordination) in silicate garnets. To date, several studies have investigated the relationship between the bulk modulus and the garnet composition. The cation substitution on the  $X$ -site is thought to result in a linear relationship between bulk modulus and composition (Beyer et al., 2021; Chai et al., 1997; Fan, Xu, Ma, Liu, & Xie, 2015; Huang & Chen, 2014; Milani et al., 2015; O'Neill et al., 1989) but nonlinear relationship was also suggested by studies on solid solutions containing grossular (Du et al., 2015; Xu et al., 2019), which is consistent with the fact that the incorporation of grossular has been shown to cause excess volume for garnet solid solutions (e.g., Bosenick & Geiger, 1997; Du et al., 2016; Ganguly et al., 1993). For the cation substitution on the  $Y$ -site, the results of previous studies on the  $Grs$ - $Adr$  solid solution also show discrepancies in the bulk modulus-composition relationship. The BLS study by Wei et al. (2021) and the high- $P$  X-ray diffraction study by Fan et al. (2017) suggested that the bulk modulus of the  $Grs$ - $Adr$  solution changes linearly with composition, while the RPR study indicated that the bulk moduli of the intermediate  $Grs$ - $Adr$  composition significantly deviate from the linearity (Babuška et al., 1978; Bass, 1986; O'Neill et al., 1989).

Natural Cr-pyrope as a major mineral of the SCLM has cation substitutions on both the  $X$ - (e.g.,  $Mg^{2+}/Fe^{2+}/Ca^{2+}$ ) and  $Y$ -site (e.g.,  $Al^{3+}/Cr^{3+}$ ). So far, studies on the elastic properties of binary  $Uvr$ - $Adr$  or  $Uvr$ - $Grs$  solid solutions are unavailable, thus the effects of Cr-substitution on the elastic properties are not clear. Furthermore, it remains unclear whether the elastic properties of Cr-pyrope at high  $P$ - $T$  can be calculated from the end-member elastic properties based on a linear dependence with composition. Although the elastic properties of end-member garnets related to Cr-pyrope have been measured both at high  $P$  and high  $T$  (e.g., Arimoto et al., 2015; Bass, 1989; Fan, Xu, Ma, Wei, et al., 2015; Gréaux & Yamada, 2019; Isaak et al., 1992; Milani et al., 2017; Sinogeikin & Bass, 2000), the elastic properties of Cr-pyrope have been measured only at room  $P$ - $T$  and high  $T$  in two separate studies (Babuška et al., 1978; Suzuki & Anderson, 1983). Therefore, it is necessary to measure the elasticity of Cr-pyrope at high  $P$  and high  $T$  to examine whether the elastic properties of Cr-pyrope can be accurately calculated using a linear interpolation of end-member elastic properties.

Before measuring the elasticity of Cr-pyrope, it is necessary to know the major element compositional characteristics of the SCLM Cr-pyrope, which helps to choose a proper Cr-pyrope sample to measure. Here, we calculated the mineral proportions and mineral compositions of the average Archon, Proton and Tecton (Table S1 in Supporting Information S1; Griffin et al., 2009) along the SCLM  $P$ - $T$  geotherms (Deen et al., 2006) using the *Perple\_X* software package (Connolly, 2005). A detailed description of the calculation is shown in the next section. The results (Figures S1–S3 and Table S2 in Supporting Information S1) indicate that the Cr-pyropes of the Archon, Proton, and Tecton contain 4–14 mol. % Uvr + Knr, 5–11 mol. % Uvr + Knr, and 5–7 mol. % Uvr + Knr, respectively. Therefore, in this study, we obtained the single-crystal elastic properties of a natural Cr-pyrope ( $\text{Prp}_{71.0}\text{Alm}_{12.6}\text{Sps}_{0.7}\text{Grs}_{3.5}\text{Uvr}_{12.2}$ ) containing 12.2 mol. % Uvr at high  $P$  and high  $T$  using the BLS method, and we examined whether the elastic properties of Cr-pyrope can be reasonably calculated using a linear interpolation of end-member elastic properties. Furthermore, we discussed the effects of chemical evolutions on the density and velocities of the SCLM.

## 2. Sample and Method

A natural single-crystal Cr-pyrope was extracted from lamproite in Zhenyuan, Guizhou Province, China. Its chemical composition was determined by electron microprobe analysis using a JXA 8230, operating at an acceleration voltage of 15 kV, with a beam current of 20 nA, and a focused electron beam of approximately 5  $\mu\text{m}$ . The results are shown in Table S3 of Supporting Information S1, and the composition of the Cr-pyrope expressed in end-member molar percentages is  $\text{Prp}_{71.0}\text{Alm}_{12.6}\text{Sps}_{0.7}\text{Grs}_{3.5}\text{Uvr}_{12.2}$ . In the following pages, we designate this Cr-pyrope Prp-Cr#12 for simplicity.

The high- $P$  and high- $T$  BLS measurements were carried out at the 13-BM-D beamline station of the Advanced Photon Source, Argonne National Laboratory. The high- $P$  BLS up to 11.0 GPa ( $\sim 2$  GPa pressure interval) was performed with a short symmetric diamond anvil cell (DAC) equipped with a pair of 500- $\mu\text{m}$ -culet diamonds. A rhenium gasket was pre-indented to a thickness of  $\sim 60$   $\mu\text{m}$  by the diamond anvils, and a 350- $\mu\text{m}$  hole was subsequently laser-drilled in the indented area and was used as the sample chamber. Then, the selected crystal, which was double-side polished with random orientation to  $\sim 20$ - $\mu\text{m}$  thickness and was square shape (side length of  $\sim 80$   $\mu\text{m}$ ), was loaded into the sample chamber together with a ruby sphere which served as the pressure marker at high  $P$  (H. Mao et al., 1986). Neon was then loaded as pressure medium, using the COMPRES/GSECARS gas-loading system (Rivers et al., 2008). The high- $T$  BLS from room  $T$  to 800 K (100 K temperature interval) was performed with an externally heated DAC (EHDAC) which was a BX90 DAC equipped with a micro resistive heater made from alumina ceramic and Pt wires and a K-type thermocouple attached to one of the anvils approximately 500  $\mu\text{m}$  away from the diamond culet. The sample chamber and single-crystal sample were prepared in the same way as what we did for the high- $P$  BLS measurements.

The sample orientation was determined by single-crystal X-ray diffraction (XRD) at the beamline station with an incident X-ray beam of 0.3344  $\text{\AA}$  wavelength focused to a beam size of  $3 \times 7$   $\mu\text{m}^2$ . The diffraction images were acquired using a stationary Perkin-Elmer area detector. At each  $P$ - $T$ , a series of  $\omega$ -scan steps, with one-degree step and exposure time of 5 s per degree, were collected. The  $\omega$  rotation axis was vertical and perpendicular to the incident beam. The ATREX software package (Dera et al., 2013) was used to analyze the diffraction images.

The BLS spectra were collected in a symmetric forward-scattering geometry with an external scattering angle ( $\theta$ ) of  $50.0^\circ$  and a JRS six-pass tandem Fabry-Pérot interferometer. A Coherent Verdi V2 solid-state laser with a wavelength of 532 nm was used, and the laser beam size was  $\sim 15$   $\mu\text{m}$  in diameter. At each  $P$ - $T$ , BLS spectra were collected at 10 different crystallographic directions from 0 to  $90^\circ$  of the azimuthal angle at every  $10^\circ$ , which was sufficient to determine the three elastic moduli ( $C_{11}$ ,  $C_{12}$ , and  $C_{44}$ ) of garnet. The measured Brillouin frequency shifts of the crystal were first converted to the compressional ( $V_p$ ) and shear ( $V_s$ ) wave velocities using the equation:

$$V_{p,s} = \lambda_0 \Delta\nu_B / (2 \sin(\theta/2)), \quad (1)$$

where the  $\lambda_0$  is the incident laser wavelength, the  $\Delta\nu_B$  is the Brillouin frequency shift, and the  $\theta$  is the external scattering angle. Then the individual elastic moduli ( $C_{11}$ ,  $C_{12}$ , and  $C_{44}$ ) were obtained by fitting the measured velocity-orientation data to the Christoffel's equation:

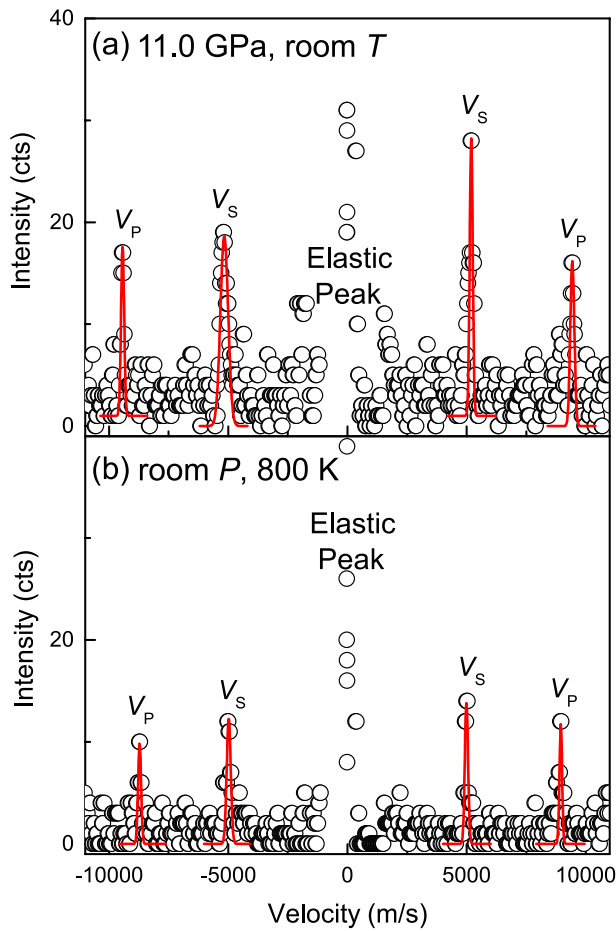


**Figure 1.** Representative Brillouin spectrum of Cr-pyropite at high  $P$  and high  $T$ . (a) 11.0 GPa and room  $T$ ; (b) room  $P$  and 800 K. The collected data and fitted results are represented by circles and red solid lines, respectively.

cubic,  $K_S(V) = (C_{11} + 2C_{12})/3$  and  $K_S(R) = (3S_{11} + 6S_{12})^{-1}$ , where  $V$  and  $R$  represent the Voigt and Reuss average scheme, respectively, and  $S_{11}$  and  $S_{12}$  are elastic compliances. Since  $S_{11} = (C_{11} + C_{12})/((C_{11} - C_{12})(C_{11} + 2C_{12}))$  and  $S_{12} = -C_{12}/((C_{11} - C_{12})(C_{11} + 2C_{12}))$ ,  $K_S(R) = (C_{11} + 2C_{12})/3$ .  $K_S(\text{VRH}) = 0.5(K_S(V) + K_S(R))$ .  $G(V) = (C_{11} - C_{12} + 3C_{44})/5$ ,  $G(R) = 5(C_{11} - C_{12})C_{44}/(4C_{44} + 3C_{11} - 3C_{12})$ , and  $G(\text{VRH}) = 0.5(G(V) + G(R))$  (Duffy, 2018). We obtained  $K_S = 167.7(8)$  GPa and  $G = 91.5(5)$  GPa at room  $P$ - $T$  for Prp-Cr#12. The aggregate compressional ( $V_P = 8.85(1)$  km/s) and shear ( $V_S = 4.97(1)$  km/s) velocities were calculated using the derived  $K_S$ ,  $G$ , and  $\rho$  to the equations:

$$V_P = \sqrt{\frac{K_S + \frac{4G}{3}}{\rho}}, \quad (3)$$

$$V_S = \sqrt{\frac{G}{\rho}}. \quad (4)$$

Using the same method, the  $C_{ij}$ ,  $K_S$ ,  $G$ ,  $V_P$ , and  $V_S$  of Prp-Cr#12 at each  $P$ - $T$  were obtained, which are shown in Tables 1 and 2 and Figures 3–5.

All the elastic moduli ( $C_{ij}$ ,  $K_S$  and  $G$ ) of Prp-Cr#12 follow a linear increase/decrease with  $P/T$  (Figures 3 and 4). The pressure derivatives of aggregate moduli ( $(\partial K_S/\partial P)_T$  and  $(\partial G/\partial P)_T$ ) are obtained by fitting the moduli obtained at high  $P$  to the third-order finite-strain equation (Birch, 1978), and the  $K_{S0}$  and  $G_0$  were fixed at the

$$|C_{ijkl}n_i n_j - \rho V_{P,S}^2 \delta_{ik}| = 0, \quad (2)$$

using the least square method (Every, 1980), where  $C_{ijkl}$  is written in full suffix notation in this equation but its reduced notation  $C_{ij}$  is used when we report the values,  $n_i$  and  $n_j$  are the direction cosines of the phonon wave vector,  $\rho$  is the density, and  $\delta_{ik}$  is the Kronecker delta function. Density at each  $P$ - $T$  was determined by collecting XRD data before and after the collection of BLS data.

$P$ - $T$  pseudosections for the average Archon, Proton and Tecton SCLMs were constructed using the Perple\_X software package (Connolly, 2005) and an internally consistent thermodynamic database for minerals (hp633ver.dat, Holland & Powell, 2011). The bulk compositions for the Archon, Proton and Tecton were from Griffin et al. (2009), which are also shown in Table S1 of Supporting Information S1. The following thermodynamic solid-solution models (Holland et al., 2018) were used for the calculations: O (HGP) for olivine, Opx (HGP) for orthopyroxene, Cpx (HGP) for clinopyroxene and Gt (HGP) for Cr-pyropite. The temperature ranges are 830–1500 K, 1030–1600 K, and 1270–1800 K for the Archon, Proton, and Tecton, respectively, while the pressure ranges are the same (3–8 GPa) for all the three SCLMs. The calculated pseudosections are shown in Figure S1 of Supporting Information S1. The mineral proportions and compositions of the Archon, Proton, and Tecton along their geotherms are shown in Table S2 of Supporting Information S1.

### 3. Results

Typical Brillouin spectra at high  $P$  and high  $T$  are shown in Figure 1. At each  $P$ - $T$ , Brillouin spectra were collected in 10 different directions, thus yielding velocities in 10 different directions (Figure 2). Individual elastic moduli ( $C_{ij}$ ) of Prp-Cr#12 (Tables 1 and 2) at each  $P$ - $T$  were obtained by fitting the corresponding velocity-orientation data to Equation 2. At room  $P$ - $T$ , we obtained  $C_{11} = 291.4(6)$  GPa,  $C_{12} = 105.9(4)$  GPa, and  $C_{44} = 90.6(3)$  GPa. The aggregate bulk ( $K_S$ ) and shear ( $G$ ) moduli were calculated using the Voigt-Reuss-Hill (VRH) average scheme (Hill, 1952). For garnet, which is

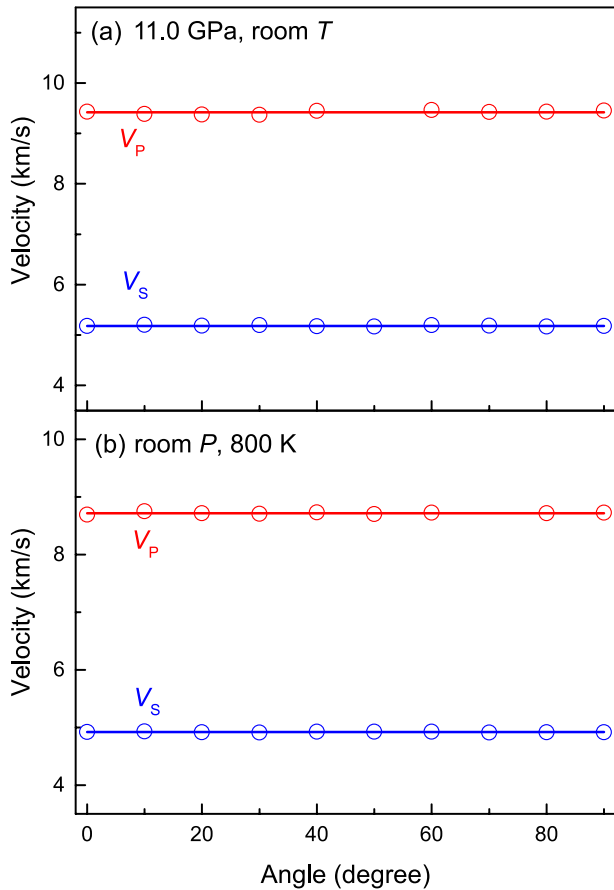


**Figure 2.** Representative acoustic velocities of Cr-pyrope at high  $P$  and high  $T$ . (a) 11.0 GPa and room  $T$ ; (b) room  $P$  and 800 K. The measured velocities and fitted results are represented by circles and solid lines, respectively.

values measured at room  $P$ - $T$  when we performed the fitting. The  $(\partial K_S/\partial P)_T$  and  $(\partial G/\partial P)_T$  were determined to be 4.3(1) and 1.4(1). The temperature derivatives of  $K_S$  ( $(\partial K_S/\partial T)_P$ ) and  $G$  ( $(\partial G/\partial T)_P$ ) were determined by linear fitting of the high- $T$  data, resulting in  $(\partial K_S/\partial T)_P = -0.0175(1)$  GPa/K and  $(\partial G/\partial T)_P = -0.0073(1)$  GPa/K.

The density data (Figure 6) collected at high  $P$  and high  $T$  were fitted to the third-order Birch-Murnaghan equation of state (BM3 EoS; Birch, 1947) combined with the thermal- $P$  model proposed by Holland and Powell (2011) using the Eosfit7c software package (Angel et al., 2014), in order to obtain the EoS parameters. The BM3 EoS was chosen for the EoS fitting as the pressure derivative of bulk modulus ( $(\partial K_T/\partial P)_T$ ) of garnet is often larger than 4. Figure 6a shows that the BM3 EoS is a good choice for fitting the high- $P$  data. The thermal EoS fitting yielded the following EoS parameters: density at zero  $P$  ( $\rho_{T0} = 3.6968(5)$  g/cm<sup>3</sup>), isothermal bulk modulus at zero  $P$  ( $K_{T0} = 168.7(25)$  GPa),  $(\partial K_T/\partial P)_T = 4.1(5)$ , and thermal expansion coefficient ( $\alpha_0 = 2.82(4) \times 10^{-5}$  K<sup>-1</sup>). The Einstein temperature ( $\theta_E = 514$  K) was calculated according to the method described by Holland and Powell (2011).

## 4. Discussion

### 4.1. Comparison With Previous Studies

We first compared the elastic moduli of Prp-Cr#12 with literature values of Prp<sub>100</sub> (Table S4 in Supporting Information S1). Up to date, a few studies have reported the elastic properties of pyrope obtained by BLS (Fan et al., 2019; Leitner et al., 1980; O'Neill et al., 1991; Sinogeikin & Bass, 2000, 2002) or UI (Chantel et al., 2016; Chen et al., 1999; Gwanmesia et al., 2006, 2007; Zou, Irifune, et al., 2012) methods. The  $C_{ij}$  of anhydrous pyrope at room  $P$ - $T$  have been reported by three BLS studies (Leitner et al., 1980; Sinogeikin & Bass, 2000, 2002). Except for the results reported by Leitner et al. (1980), the other two studies reported consistent values of  $C_{ij}$ , and  $C_{11} = 297(3)$ – $298(3)$  GPa,  $C_{12} = 107(2)$ – $108(2)$  GPa and  $C_{44} = 93(2)$ – $93(2)$  GPa. Two BLS measurements performed on hydrous pyrope indicated that several hundred ppm water has no discernible effect on the elasticity of pyrope (Fan et al., 2019; O'Neill et al., 1991). In this study we obtained  $C_{11} = 291.4(6)$  GPa,  $C_{12} = 105.9(4)$  GPa, and  $C_{44} = 90.6(3)$  GPa for Prp-Cr#12 at room  $P$ - $T$ . Therefore, the values of  $C_{11}$ ,  $C_{12}$ , and  $C_{44}$  of Prp-Cr#12 are very close to the  $C_{11}$ ,  $C_{12}$ , and  $C_{44}$  of the anhydrous pyropes (Sinogeikin & Bass, 2000, 2002) within the uncertainty. Since the  $C_{ij}$  between the Prp<sub>100</sub> and the Prp-Cr#12 is close, their aggregated moduli ( $K_S = 167.7(8)$ – $171(2)$  GPa and  $G = 91.5(5)$ – $94(2)$  GPa) are also comparable (Table S4 in Supporting Information S1).

**Table 1**  
Single-Crystal Elastic Properties of the Cr-Pyrope at Room  $T$  and High  $P$

Pressure (GPa)	$C_{11}$ (GPa)	$C_{12}$ (GPa)	$C_{44}$ (GPa)	$K_S$ (GPa)	$G$ (GPa)	$V_p$ (km/s)	$V_s$ (km/s)	Density (g/cm <sup>3</sup> )
0.0001	291.4(6)	105.9(4)	90.6(3)	167.7(8)	91.5(5)	8.85(1)	4.97(1)	3.6973(7)
0.5(1)	295.1(6)	107.7(5)	91.2(5)	170.2(8)	92.2(6)	8.89(1)	4.99(1)	3.7080(8)
1.5(1)	300.9(5)	110.8(4)	92.5(6)	174.2(9)	93.5(5)	8.95(1)	5.01(1)	3.7295(7)
2.2(1)	305.2(8)	113.1(6)	93.6(5)	177.1(7)	94.6(6)	9.00(1)	5.03(1)	3.7433(9)
4.6(1)	318.4(7)	121.1(4)	97.1(4)	186.9(7)	97.7(6)	9.14(1)	5.08(1)	3.7931(7)
6.8(1)	332.3(9)	128.5(7)	99.9(4)	196.4(8)	100.7(5)	9.28(1)	5.12(1)	3.8380(8)
9.1(1)	346.1(8)	135.9(5)	103.2(6)	206.0(9)	104.0(7)	9.42(1)	5.18(1)	3.8823(9)
11.0(1)	355.4(6)	141.7(8)	105.3(4)	212.9(8)	105.9(7)	9.51(1)	5.20(1)	3.9164(10)



**Table 2**  
Single-Crystal Elastic Properties of the Cr-Pyrope at Room  $P$  and High  $T$

Temperature (K)	$C_{11}$ (GPa)	$C_{12}$ (GPa)	$C_{44}$ (GPa)	$K_S$ (GPa)	$G$ (GPa)	$V_p$ (km/s)	$V_s$ (km/s)	Density ( $\text{g/cm}^3$ )
296	291.4(5)	105.9(5)	90.6(4)	167.7(7)	91.5(5)	8.85(1)	4.97(1)	3.6973(7)
400	289.1(6)	104.5(4)	89.8(4)	166.0(7)	90.8(6)	8.83(1)	4.96(1)	3.6850(7)
500	286.4(5)	103.1(6)	89.1(3)	164.2(7)	90.1(5)	8.80(1)	4.95(1)	3.6724(6)
600	283.8(8)	101.8(4)	88.2(5)	162.5(7)	89.3(6)	8.77(1)	4.94(1)	3.6588(7)
700	281.2(7)	100.4(7)	87.3(4)	160.7(7)	88.5(5)	8.74(1)	4.93(1)	3.6469(7)
800	278.9(8)	99.1(7)	86.5(5)	159.0(8)	87.8(6)	8.72(1)	4.92(1)	3.6348(6)

To date, five UI studies (Chantel et al., 2016; Chen et al., 1999; Gwanmesia et al., 2006, 2007; Zou, Irifune, et al., 2012) have reported  $K_S$  and  $G$  of Prp<sub>100</sub> at room  $P$ - $T$ , and these values except those reported by Gwanmesia et al. (2006) are very consistent to each other ( $K_S = 170.0(2)$ – $172.0(16)$  GPa and  $G = 89.1(5)$ – $93.2(1)$  GPa) and are also close to the  $K_S$  and  $G$  of Prp-Cr#12 obtained in this study.

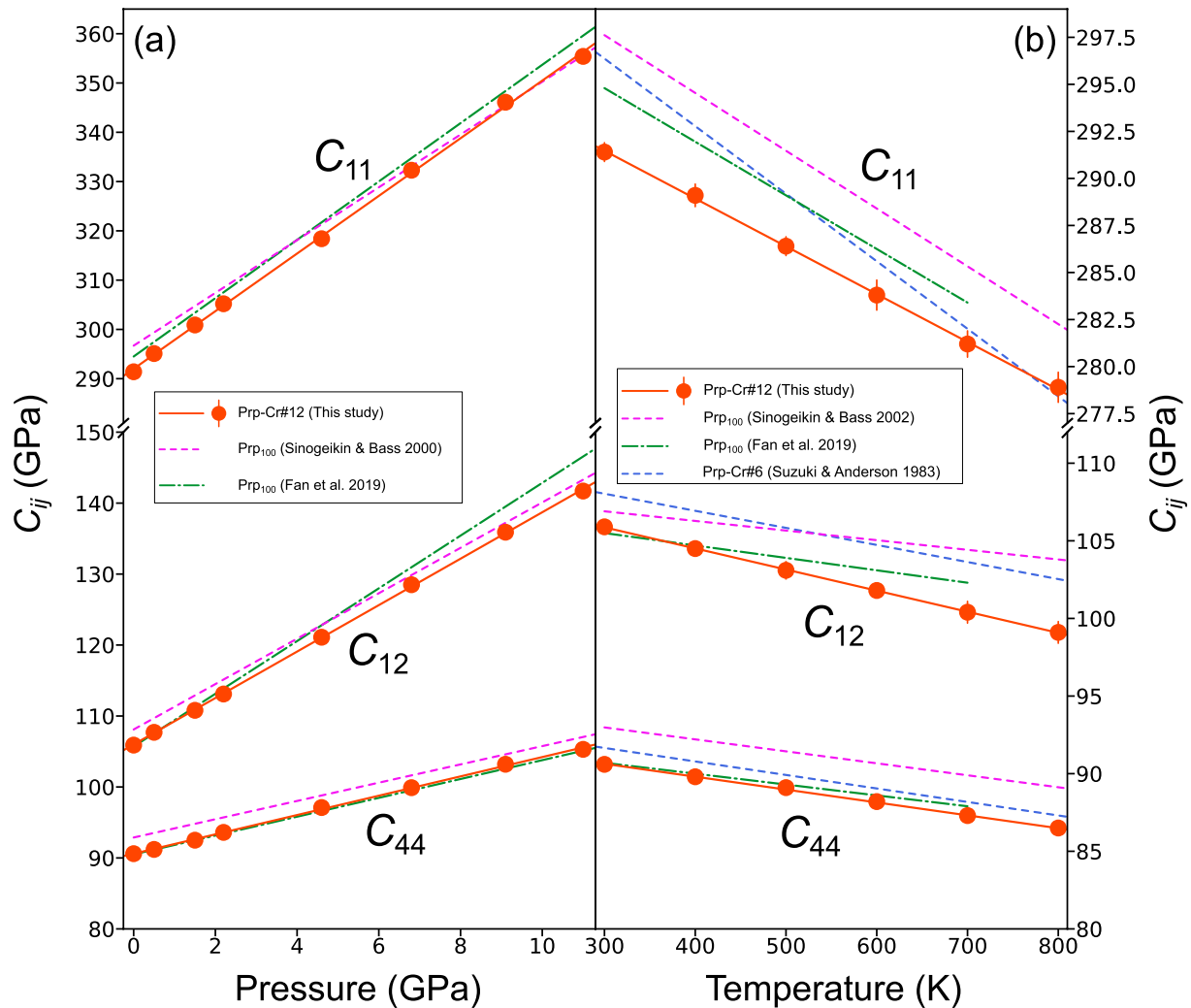


**Figure 3.** (a)  $C_{11}$ ,  $C_{12}$ , and  $C_{44}$  of Cr-pyrope at high  $P$  and (b) high  $T$  in this study are compared with those of previous studies (Fan et al., 2019; Sinogeikin and Bass, 2000, 2002; Suzuki & Anderson, 1983). The error bars may be smaller than the symbol size. Prp-Cr#12 = Prp<sub>71.0</sub>Alm<sub>12.6</sub>Sp<sub>0.7</sub>Gr<sub>3.5</sub>Uvr<sub>12.2</sub>; Prp<sub>100</sub> = pyrope; Prp-Cr#6 = Prp<sub>72.6</sub>Alm<sub>15.7</sub>Gr<sub>0.6</sub>Adr<sub>4.3</sub>Sp<sub>0.7</sub>Uvr<sub>6.1</sub>.

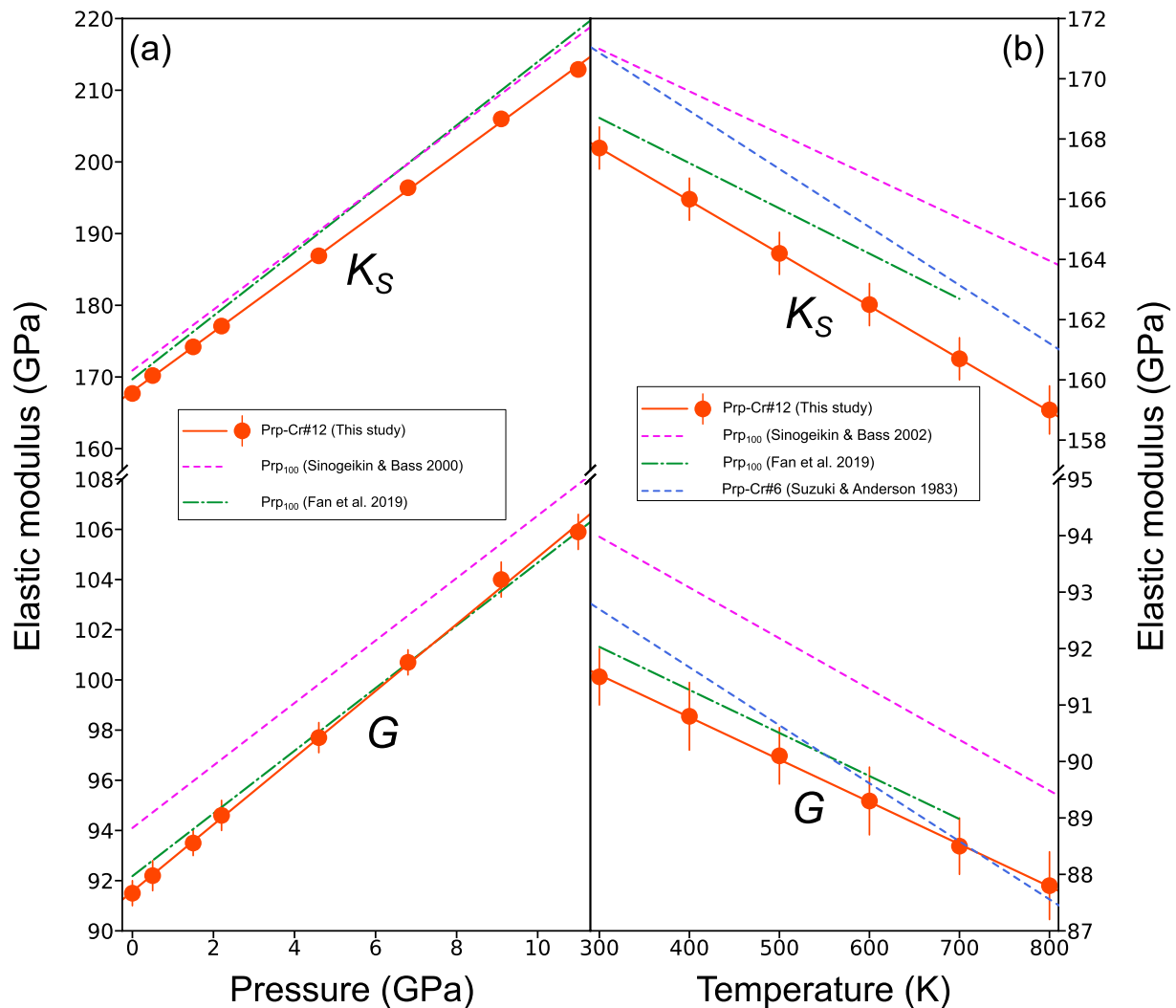


**Figure 4.** (a)  $K_S$  and  $G$  of Cr-pyrope at high  $P$  and (b) high  $T$  in this study are compared with previous studies (Fan et al., 2019; Sinogeikin & Bass, 2000, 2002; Suzuki & Anderson, 1983). The error bars may be smaller than the symbol size. Prp-Cr#12 = Prp<sub>71.0</sub>Alm<sub>12.6</sub>Sps<sub>0.7</sub>Grs<sub>3.5</sub>Uvr<sub>12.2</sub>; Prp<sub>100</sub> = pyrope; Prp-Cr#6 = Prp<sub>72.6</sub>Alm<sub>15.7</sub>Grs<sub>0.6</sub>Adr<sub>4.3</sub>Sps<sub>0.7</sub>Uvr<sub>6.1</sub>.

Suzuki and Anderson (1983) reported  $C_{11} = 296.6(15)$  GPa,  $C_{12} = 108.5(16)$  GPa,  $C_{44} = 91.6(2)$  GPa,  $K_S = 171.2(8)$  GPa, and  $G = 92.6(3)$  GPa for a natural Cr-pyrope (Prp-Cr#6) at room  $P$ - $T$ , and these values are very close to the  $C_{ij}$ ,  $K_S$ , and  $G$  of Prp-Cr#12 obtained in this study within the uncertainty. Babuška et al. (1978) reported  $K_S = 170.0(18)$ – $171.6(13)$  GPa and  $G = 90.7(1)$ – $92.6(2)$  GPa for four natural Cr-pyropes (Cr# = 5–9) at room  $P$ - $T$ , and these values are quite consistent with the results reported by Suzuki and Anderson (1983) and those presented in this study. Therefore, the compositional variation in natural Cr-pyropes seems to have no significant effect on the room  $P$ - $T$  elastic moduli and the elastic moduli of Cr-pyropes are very close to Prp<sub>100</sub> (Table S4 in Supporting Information S1).

The pressure derivative of  $K_S$  ( $(\partial K_S/\partial P)_T = 4.3(1)$ ) and  $G$  ( $(\partial G/\partial P)_T = 1.4(1)$ ) of Prp-Cr#12 obtained in this study are very close to the  $(\partial K_S/\partial P)_T$  (4.1(3)) and  $(\partial G/\partial P)_T$  (1.3(2)) of anhydrous Prp<sub>100</sub> obtained by BLS method (Sinogeikin & Bass, 2000) within the uncertainty, respectively. Four UI studies have reported  $(\partial K_S/\partial T)_P$  and  $(\partial G/\partial T)_P$  for anhydrous Prp<sub>100</sub> (Chantel et al., 2016; Chen et al., 1999; Gwanmesia et al., 2006; Zou, Irifune, et al., 2012). As shown in Table S4 of Supporting Information S1, Chen et al. (1999) reported much higher  $(\partial K_S/\partial P)_T$  (5.3(4)) than the BLS results, and the other three studies reported more close values (4.3(3)–4.51(2)) to the BLS results. The UI studies reported slightly higher values of  $(\partial G/\partial P)_T$  (1.5(2)–1.66(5)) than those of the BLS

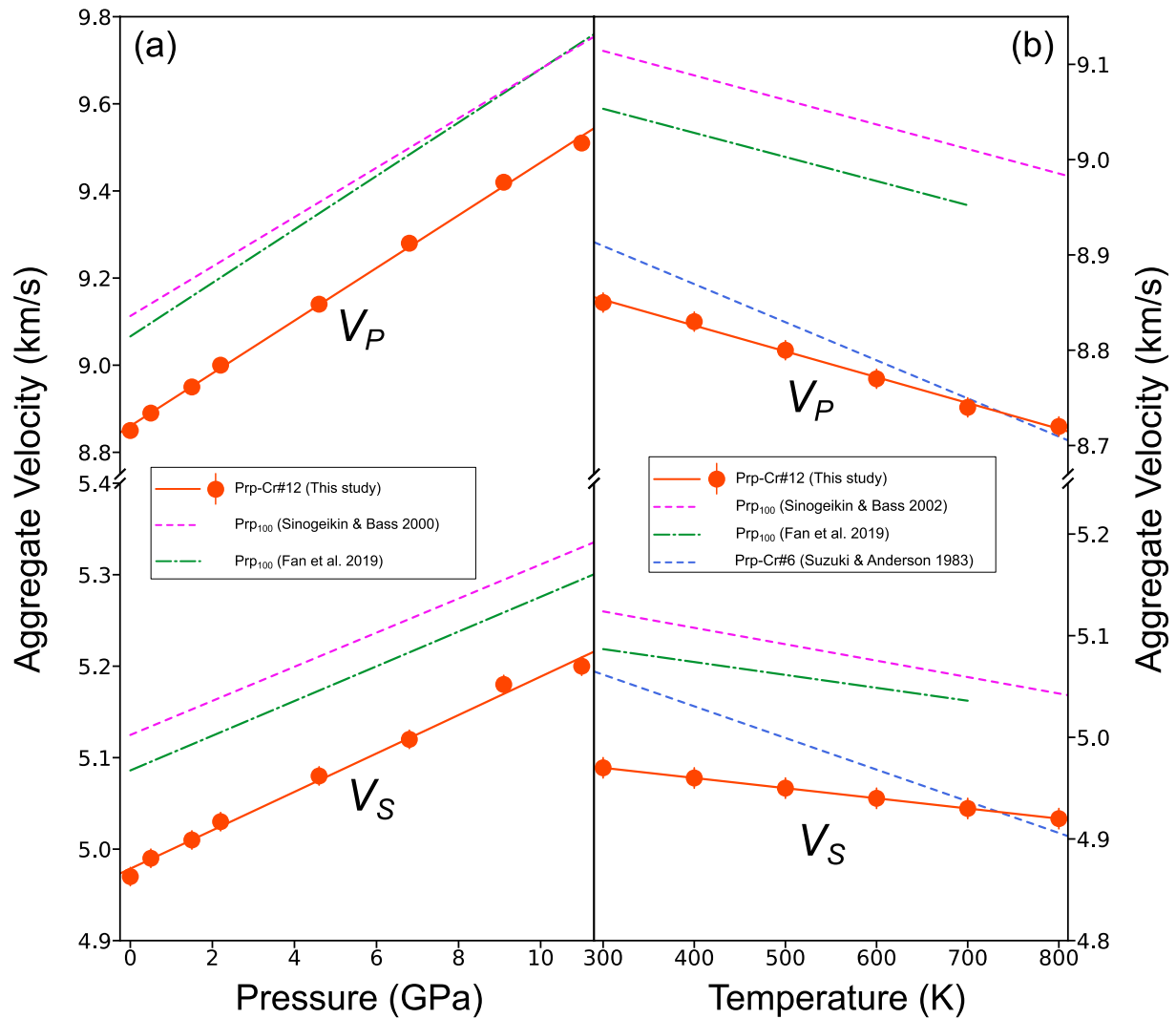


**Figure 5.** (a)  $V_P$  and  $V_S$  of Cr-pyrope at high  $P$  and (b) high  $T$  in this study are compared with previous studies (Fan et al., 2019; Sinogeikin & Bass, 2000; Zou, Irifune, et al., 2012). The error bars may be smaller than the symbol size. Prp-Cr#12 = Prp<sub>71.0</sub>Alm<sub>12.6</sub>Sps<sub>0.7</sub>Grs<sub>3.5</sub>Uvr<sub>12.2</sub>; Prp<sub>100</sub> = pyrope; Prp-Cr#6 = Prp<sub>72.6</sub>Alm<sub>15.7</sub>Grs<sub>0.6</sub>Adr<sub>4.3</sub>Sps<sub>0.7</sub>Uvr<sub>6.1</sub>.

results. Therefore, our results of  $(\partial K_S/\partial P)_T$  and  $(\partial G/\partial P)_T$  are close to previous BLS values of anhydrous Prp<sub>100</sub>, indicating that such composition variation does not influence the  $(\partial K_S/\partial T)_P$  and  $(\partial G/\partial P)_T$  significantly.

The temperature derivative of  $K_S$  ( $(\partial K_S/\partial T)_P = -0.0175(1)$  GPa/K) of Prp-Cr#12 is slightly smaller than that of anhydrous Prp<sub>100</sub> ( $-0.014(2)$  GPa/K; Sinogeikin & Bass, 2002) obtained by BLS method. The UI studies (Chantel et al., 2016; Gwanmesia et al., 2007; Zou, Irifune, et al., 2012) reported  $(\partial K_S/\partial T)_P = -0.0193(4) - -0.0170(1)$  GPa/K which are very close to the value of Prp-Cr#12 obtained in this study. The temperature derivative of  $G$  ( $(\partial G/\partial T)_P = -0.0073(1)$  GPa/K) is close to the values of Prp<sub>100</sub> ( $-0.009(1) - -0.008(1)$  GPa/K) obtained by the BLS method (Fan et al., 2019; Sinogeikin & Bass, 2002); Chantel et al. (2016) reported  $(\partial G/\partial T)_P = -0.008(1)$  GPa/K for Prp<sub>100</sub> obtained by UI method, which is close to  $(\partial G/\partial T)_P$  of Prp-Cr#12 obtained in this study. However, using the same method, Gwanmesia et al. (2007) and Zou, Irifune, et al. (2012) reported smaller values of  $(\partial G/\partial T)_P$  ( $-0.0107(1) - -0.0104(2)$  GPa/K) for Prp<sub>100</sub>. Suzuki and Anderson (1983) reported for Prp-Cr#6  $(\partial K_S/\partial T)_P = -0.0193(2)$  GPa/K and  $(\partial G/\partial T)_P = -0.0102(1)$  GPa/K, which are smaller than the values of Prp-Cr#12 obtained in this study.

The EoS fitting of our XRD data of Prp-Cr#12 yielded  $K_{70} = 168.7(25)$  GPa and  $\alpha_0 = 2.82(4) \times 10^{-5}$  K<sup>-1</sup>. The  $K_{70}$  was converted to  $K_{S0} = 169.3(25)$  GPa ( $K_{70} = K_{S0}/(1 + \alpha\gamma T)$ , where  $\alpha$  and  $\gamma$  are the thermal expansion coefficient



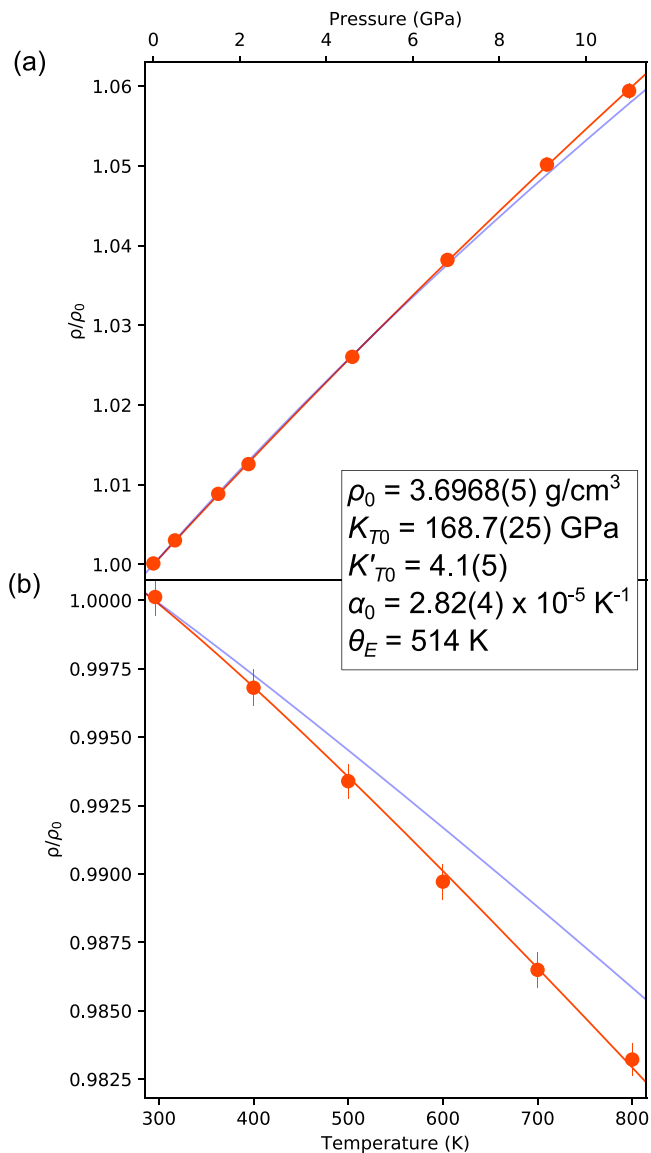


**Figure 6.** (a) Densities of Prp-Cr#12 (red circles) at high  $P$  and (b) high  $T$ . The red curves represent the thermal- $P$  EoS fit of the data. The obtained values of the EoS parameters are also shown. The blue curves represent the EoS of Prp<sub>100</sub> obtained from Milani et al. (2015).

and Grüneisen parameter, respectively), using the obtained  $\alpha_0$  from this study and  $\gamma = 1.15$  from Zou, Gréaux, et al. (2012). Although, the uncertainty of  $K_{70}$  obtained from EoS fitting is large, the  $K_{50}$  calculated from  $K_{70}$  and the measured  $K_{50}$  (167.7(8) GPa) show good agreement. As shown in Figure 6 and Table S5 in Supporting Information S1, the obtained  $\alpha_0$  for Prp-Cr#12 is larger than that of Prp<sub>100</sub>. For example, the recent high- $T$  single-crystal XRD study (Milani et al., 2015) reported  $\alpha_0 = 2.543(5) \times 10^{-5} \text{ K}^{-1}$  for Prp<sub>100</sub>, which is 9.8% smaller than the  $\alpha_0$  of Prp-Cr#12.

#### 4.2. High- $P$ and High- $T$ Elastic Properties of Cr-Pyropo Calculated Using End-Member Component Properties

To examine whether the elastic properties of Cr-pyropo at high  $P$  and high  $T$  can be calculated using the end-member component elastic properties, we calculated the elastic properties ( $\rho$ ,  $K_S$ ,  $G$ ,  $V_p$ , and  $V_S$ ) of Prp-Cr#12 at high  $P$  and high  $T$  using the directly measured elastic parameters (Table S4 in Supporting Information S1) in this study and then compared the results to those calculated using the elastic parameters interpolated from linear mixing of end-member elastic parameters (end-member model; Table S5 in Supporting Information S1; Angel et al., 2018; Arimoto et al., 2015; Bass, 1986, 1989; Cameron et al., 1973; Chantel et al., 2016; Dymshits et al., 2014; Faccincani et al., 2021; Fan et al., 2020; Gréaux & Yamada, 2019; Gwanmesia et al., 2014, 2006; Hao et al., 2020; Hugh-Jones, 1997; Isaak et al., 1992; Jackson et al., 2007; Jacobsen et al., 2010; Jeanloz & Thompson, 1983; Klemme et al., 2005; Kroll et al., 2012; Li & Neuville, 2010; Ma et al., 2009; Z. Mao et al., 2015; Milani et al., 2015, 2017; Ohashi, 1984; Sang & Bass, 2014; Sinogeikin & Bass, 2000, 2002; Soga, 1967; Tribaudino et al., 2008; Wang & Ji, 2001; Xu et al., 2018, 2020, 2022; Yang & Ghose, 1994; Zhang & Bass, 2016a, 2016b; Zhang et al., 1998; Zhao et al., 1997, 1998; Zou, Gréaux, et al., 2012). We calculated the elastic properties at pressures of 3–8 GPa at 1000 and 1600 K, which are the lower and upper bound of typical SCLM  $P$ - $T$  conditions where garnet-peridotite stabilizes. At high  $P$  and high  $T$ , the density of Cr-pyropo is calculated using the thermal- $P$  EoS (Text S1 in Supporting Information S1), the  $K_S$  and  $G$  are calculated using the third-order finite strain equation (Text S2 in Supporting Information S1), and the  $V_p$  and  $V_S$  are calculated using Equations 3 and 4. The uncertainties of the calculated elastic properties are estimated based on the uncertainties of the elastic parameters.

The calculated results are shown in Figure S4 of Supporting Information S1 and Figure 7. At 8 GPa, the density of Prp-Cr#12 calculated using the directly measured elastic parameters ( $\rho_{dm}$ ) is 0.2% and 0.6% smaller than the densities calculated using the end-member model elastic parameters ( $\rho_{em}$ ) at 1000 and 1600 K, respectively. The  $K_{S, dm}$  is 1.5% and 1.3% smaller than  $K_{S, em}$  at 1000 and 1600 K, respectively. At 1000 K the  $G_{dm}$  is very close to the  $G_{em}$  (0.05% difference), while the latter is 2.0% smaller than the former at 1600 K (Figure S4 in Supporting Information S1). The differences between  $V_{p, dm}$  and  $V_{p, em}$  are 0.4% and 0.3% at 1000 and 1600 K, respectively (Figure 7). By comparison,  $V_{S, dm}$  is only 0.09% larger than  $V_{S, em}$  at 1000 K, but the latter is 1.2% smaller than the former at 1600 K (Figure 7). At 8 GPa, the uncertainties of the calculated  $\rho_{dm}$  and  $\rho_{em}$  are  $\sim 0.1\%$ , while the uncertainties of the calculated  $K_S$  and  $G$  are 2.0%–3.0%. The uncertainties of the  $V_p$  and  $V_S$  are less than 2.0% (Figure 7). Therefore, the differences between the calculated elastic properties except for the density of Prp-Cr#12 at high  $P$  and high  $T$  using the directly measured elastic parameters and those calculated using the end-member model elastic parameters are at the same level as their uncertainties (Figure S4 in Supporting Information S1 and Figure 7).

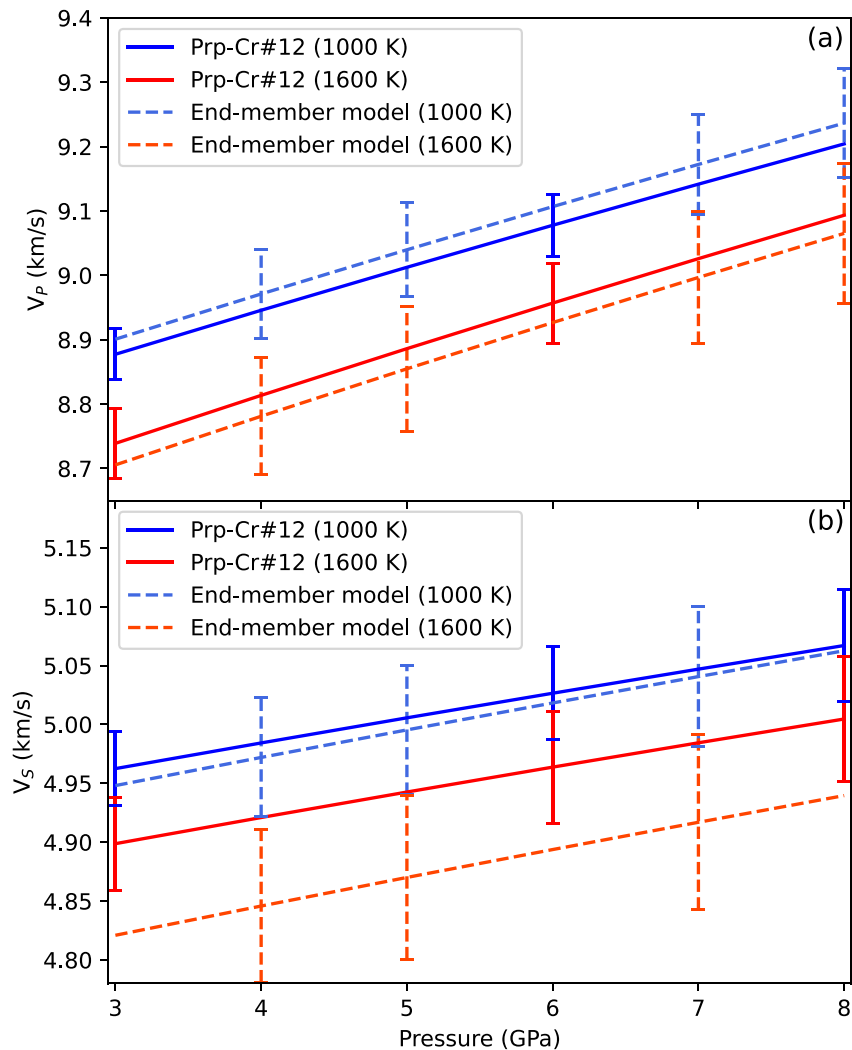


**Figure 7.** (a)  $V_p$  and (b)  $V_s$  of Prp-Cr#12 along isotherms at 1000 and 1600 K over 3–8 GPa. The solid curves represent values calculated using the elastic parameters (Table S4 in Supporting Information S1) fitted to the Prp-Cr#12 data. The dashed curves represent values calculated using the end-member model (linear average of garnet end-member parameters; Table S5 in Supporting Information S1) elastic parameters determined for the Prp-Cr#12 composition. Error bars are shown at selected pressures.

We also provide an assessment of the influence of using the end-member model elastic parameters of Cr-pyrope on the calculated density and velocity of the SCLM. We choose the mineral proportions and mineral compositions of the Proton at 6 GPa, because the composition of the Cr-pyrope at 6 GPa is very close to Prp-Cr#12 in this study (Figures S2, S3, and Table S2 in Supporting Information S1). As shown in Figure S2 of Supporting Information S1, the Proton consists of olivine, orthopyroxene, clinopyroxene and Cr-pyrope (replaced by Prp-Cr#12 in this study). We calculated the density and velocity of the Proton in two models (model#1 and model#2). In both models, the used elastic parameters of olivine, orthopyroxene and clinopyroxene are interpolated from linear mixing of their end-member component elastic parameters (Table S5 in Supporting Information S1). However, the directly measured elastic parameters of Cr-pyrope are used in model#1, while the end-member model elastic parameters of Cr-pyrope are used in model#2. At high  $P$  and high  $T$ , for each mineral, the density is calculated using the thermal- $P$  EoS (Text S1 in Supporting Information S1). The third-order finite strain equation (Text S2 in Supporting Information S1) is used to calculate the bulk moduli of olivine and Cr-pyrope and the shear modulus of Cr-pyrope, while the fourth-order finite strain equation (Text S2 in Supporting Information S1) is used to calculate the bulk moduli of orthopyroxene and clinopyroxene and the shear moduli of olivine, orthopy-

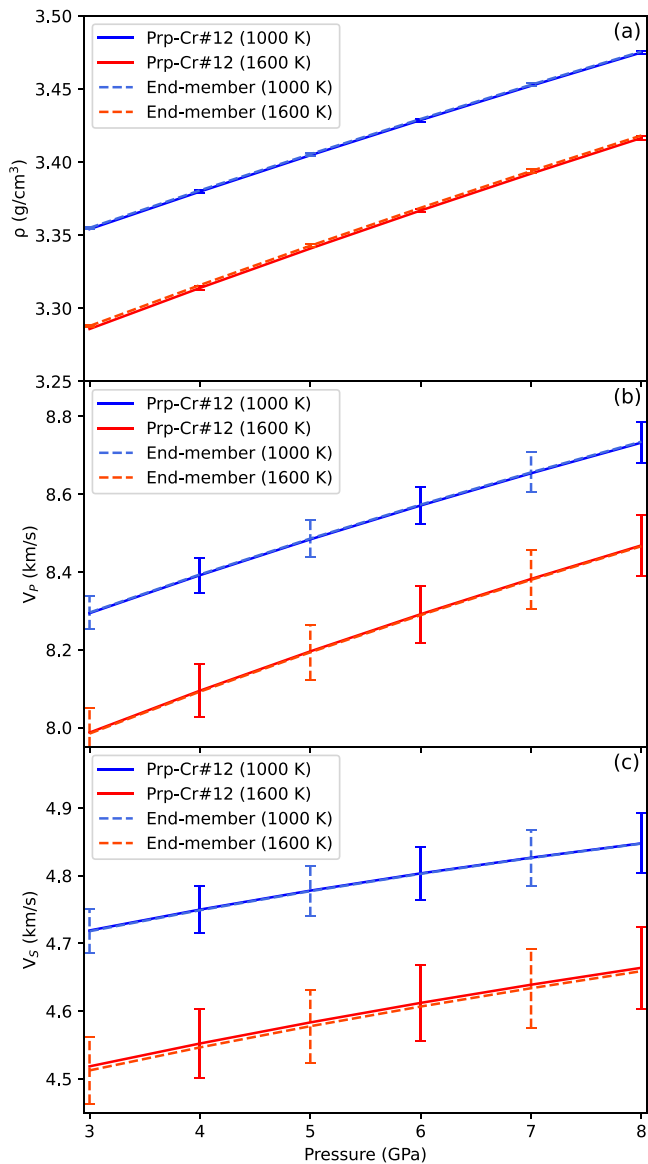


**Figure 8.** (a) Density  $\rho$ , (b) compressional  $V_p$ , and (c) shear wave velocity  $V_s$  of the Proton (Prp-Cr#12 is its Cr-pyrope) along isotherms at 1000 and 1600 K over 3–8 GPa. The solid curves represent results for which the elastic parameters (Table S4 in Supporting Information S1) fitted to the Prp-Cr#12 data are used. The dashed curves represent values for which the end-member model (linear average of garnet end-member parameters; Table S5 in Supporting Information S1) elastic parameters determined for the Prp-Cr#12 composition are used. Error bars are shown at selected pressures.

decrease to 0.2% as the  $P$  increases to 8 GPa. The differences in  $V_p$  are at the same level as the uncertainties (Figure 10a). Likewise, at 1500 K, the differences in  $V_p$  between the Archon, Proton and Tecton decrease from 1.1% at 3 GPa to 0.3% at 8 GPa. By comparison, the differences in  $V_s$  between the Archon, Proton and Tecton are  $\sim$ 0.3% under the  $P$ - $T$  conditions, which are within the uncertainty of the  $V_s$  (Figure 10b). The results indicate that the chemical evolution of the SCLM from the Archon to Tecton does not change the velocities significantly if the temperature effect is not considered.

roxene, and clinopyroxene. The density, bulk modulus and shear modulus of the mineral aggregate are calculated using the Voigt-Reuss-Hill average scheme. The velocities are then calculated using Equations 3 and 4. The density and velocity of both models are calculated at pressures of 3–8 GPa and temperatures of 1000 and 1600 K.

The calculated results are presented in Figure 8, indicating that using the end-member model elastic parameters of Cr-pyrope has very limited effects on the calculations of density and velocity of the SCLM. As shown in Figure 8, at 8 GPa and 1600 K, the differences between model#1 and model#2 are 0.05%, 0.03%, and 0.1% in the density, compressional velocity, and shear velocity, respectively, which are within their uncertainties (Figure 8). Therefore, the end-member model provides a sufficient approximation for the elastic properties of Cr-pyrope at the  $P$ - $T$  conditions of the SCLM, especially when calculating the elastic properties of the SCLM mineral aggregate.

### 4.3. Densities and Velocities of SCLM and the Compositional Effects

It is well known that the Earth's upper mantle is heterogeneous in seismological structure, which is probably associated with the heterogeneity in the lithosphere thermal and compositional structure (e.g., Li et al., 2008). The classification of SCLM into the Archon, Proton and Tecton (Griffin et al., 2009) reflects this heterogeneity to some extent. In this study, our experimental results indicate that the density and velocity of Cr-pyrope at the SCLM  $P$ - $T$  conditions can be reasonably modeled using the end-member elastic properties. In this section, we calculated the densities and velocities of the Archon, Proton and Tecton at pressures of 3–8 GPa and at temperatures of 1300 and 1500 K, in order to understand the effects of chemical evolution on the density and velocity of the SCLM. The mineral proportions and mineral compositions under the  $P$ - $T$  conditions are calculated using the Perple\_X software package (Figure S5 and Table S6 in Supporting Information S1; Connolly, 2005). The densities and velocities of each mineral and the mineral aggregates are calculated using the same method as described in Section 4.2.

The calculated densities as a function of  $P$  and  $T$  for the Archon, Proton, and Tecton are shown in Figure 9, indicating that the density of the SCLM increases from Archon to Tecton. As shown in Figure 9, at 8 GPa and 1300 K the densities of the Proton and Tecton are 1.1% and 1.8% higher than that of the Archon, respectively; at 8 GPa and 1500 K, the Archon is 1.1% and 2.4% less dense than the Proton and Tecton, respectively.

The calculated velocities as a function of  $P$  and  $T$  for the Archon, Proton, and Tecton are shown in Figures 10a and 10b, indicating that the velocities of the SCLM do not change significantly as the chemical evolution proceeds from the Archon to Tecton. As shown in Figure 10a, at 3 GPa and 1300 K, the  $V_p$  of the Archon is 0.3% and 0.8% lower than the  $V_p$  of the Proton and Tecton, respectively, and the differences between the Archon, Proton and Tecton

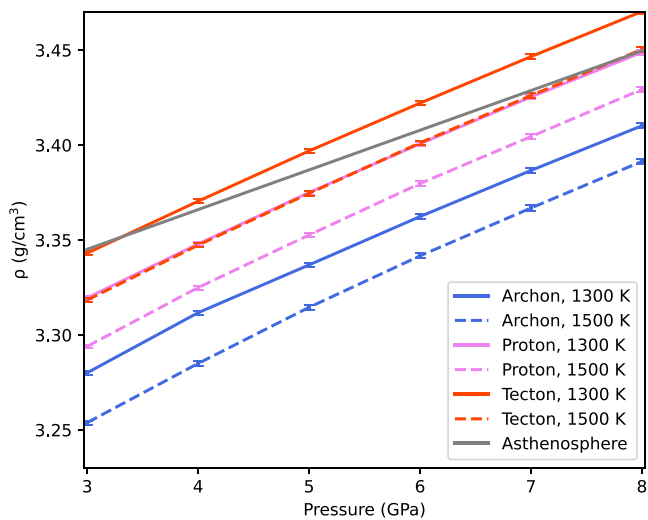


**Figure 9.** Calculated density- $P$  profiles of the Archon, Proton, and Tecton along isotherms at 1300 K (solid curves) and 1500 K (dashed curves) over the pressure range of 3–8 GPa. The density of the asthenosphere (Djomani et al., 2001) is also shown. Error bars are shown at selected pressures.

The velocity/density ratio ( $\rho/V_p$  and  $\rho/V_s$ ) of the Archon, Proton, and Tecton as a function of  $P$  are also shown in Figures 10c and 10d, indicating that, in comparison to  $V_p$  and  $V_s$ , the  $\rho/V_p$  and  $\rho/V_s$  are more sensitive to the compositional change of the SCLM, which could be used as indicators of compositional anomalies (Afonso et al., 2010; Deschamps et al., 2002; Forte & Perry, 2000). As shown in Figures 10c and 10d, at 1300 K, the  $\rho/V_p$  of the Proton and Tecton are 0.9%–1.2% and 1.1%–1.7% higher than that of the Archon within 3–8 GPa, respectively; and increasing the temperature to 1500 K increases the  $\rho/V_p$  of the Archon, Proton and Tecton by 0.5%–0.8%, 0.5%–0.7% and 0.4%–0.5% within 3–8 GPa, respectively. By comparison, at 1300 K, the  $\rho/V_s$  of the Proton and Tecton are  $\sim$ 1.4% and  $\sim$ 1.8% higher than that of the Archon within 3–8 GPa, respectively; and increasing the temperature to 1500 K increases the  $\rho/V_s$  of the Archon, Proton and Tecton by 0.8%–0.9%, 0.7%–0.9%, and 0.7%–0.8% within 3–8 GPa, respectively.

The chemical evolution of the SCLM from the Archon to Tecton is likely caused by mantle metasomatism, as suggested by dozens of studies on peridotite xenoliths from various cratons (e.g., Agashev et al., 2013; Malkovets et al., 2007; Shu & Brey, 2015; Shu et al., 2013). In addition, the temperatures of metasomatically modified peridotites are generally  $\sim$ 200 K higher than that of the original Archon (Agashev et al., 2013; Ionov et al., 2010). Therefore, the temperature increase should be considered when we investigate the effects of chemical evolution on the density and velocity of the SCLM.

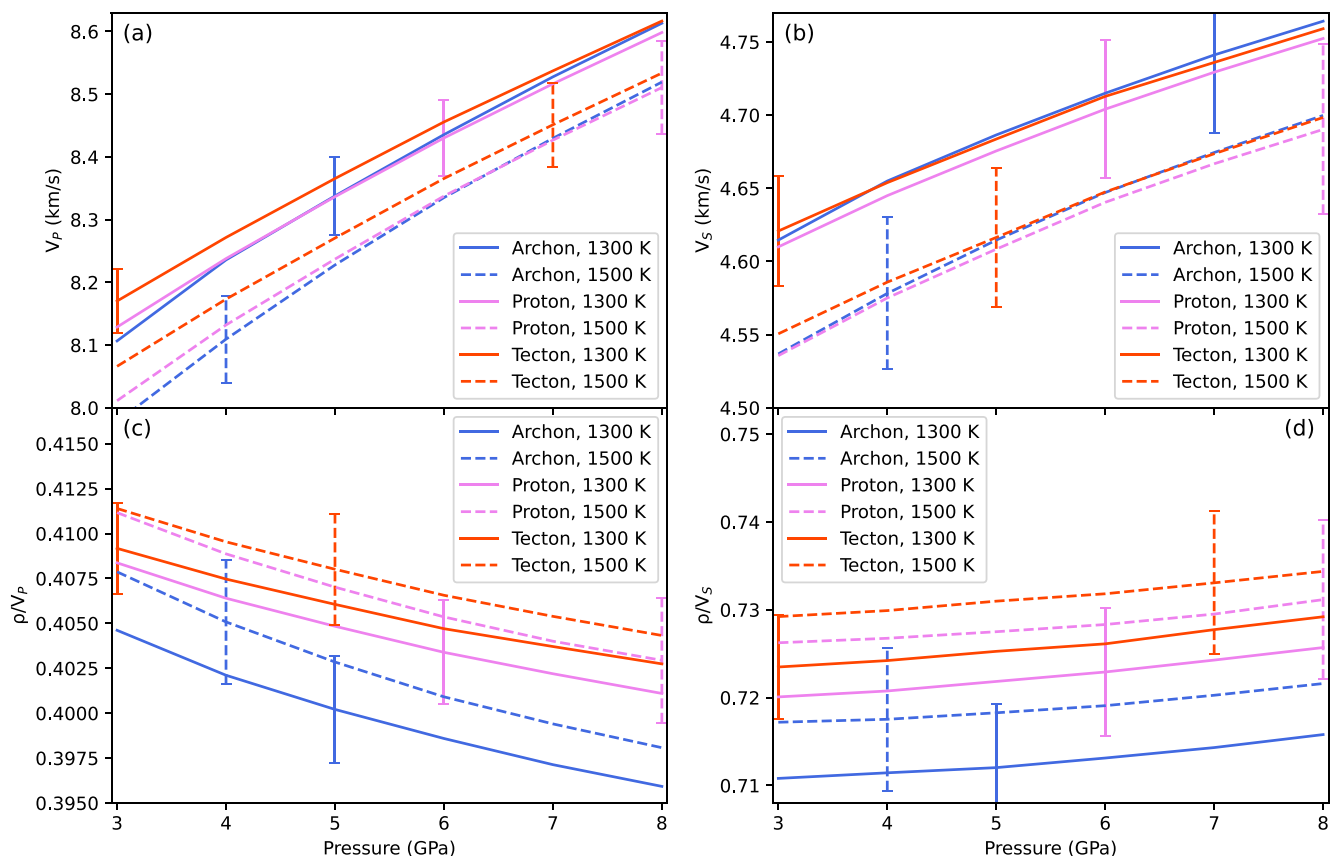


**Figure 10.** Velocity and density/velocity ratio of the Archon, Proton, and Tecton at pressures of 3–8 GPa along isotherms at 1300 K (solid curves) and 1500 K (dashed curves). (a)  $V_p$ , (b)  $V_s$ , (c)  $\rho/V_p$ , and (d)  $\rho/V_s$ . Error bars are shown at selected pressures.

Considering the temperature increase induced by metasomatism (Agashev et al., 2013; Ionov et al., 2010), the density increase induced by the compositional evolution is diminished. As shown in Figure 9, at 8 GPa the densities of the Proton and Tecton at 1500 K are  $\sim 0.6\%$  lower than their densities at 1300 K, respectively. Density is a key factor that controls the evolution of the SCLM, its increase may cause the regional gravitational instabilities and then the occurrence of delamination of the lower lithosphere into the asthenosphere when other factors like viscosity are available. Delamination was proposed to be a mechanism for the destruction of the ancient cratons, and a famous example is the destructed lithosphere under the eastern block of North China (Zhu et al., 2012). In Figure 9, the density- $P$  profile of the asthenosphere along 1600 K (Djomani et al., 2001) is shown for comparison. The density of the Archon is 1.2% lower than that of the asthenosphere at 8 GPa (Figure 9), which could have ensured the longevity of the ancient cratons (Wu et al., 2019). However, as a result of the mantle metasomatism, the Archon would evolve to the Tecton (Griffin et al., 2009), and the density of the SCLM would increase. As shown in Figure 9, at 8 GPa and 1500 K, the Proton is 0.6% less dense than the asthenosphere, while the density of the Tecton at the same  $P$ - $T$  condition is very comparable to that of the asthenosphere. At 8 GPa and 1300 K, the density of the Proton is very close to that of the asthenosphere and the Tecton is 0.6% denser than the asthenosphere. This indicates that if the composition of the Archon modified by metasomatism is comparable with that of the Tecton, the modified region of the SCLM is likely to be gravitationally unstable during the cooling process, which would facilitate the subsequent delamination.

Although the chemical evolution of the SCLM from the Archon to Tecton does not change the velocities significantly, the metasomatism of the SCLM can cause a low-velocity feature due to the temperature increase through the metasomatic process. As shown in Figures 10a and 10b, the 200 K temperature increase would cause 1.0%–1.6% and 1.3%–1.7% decreases in the  $V_p$  and  $V_s$ , respectively. Therefore, the mantle metasomatism could cause low-velocity anomalies within the SCLM, but the anomalies essentially originate from the temperature variation. The low- $V_s$  anomalies ( $\sim 1\%$ ) observed beneath some cratons such as the Kaapvaal craton (Fouch et al., 2004) could be explained by the metasomatic modification of the original Archon. As increasing temperature increases the  $\rho/V_p$  and  $\rho/V_s$ , the differences between the Archon, Proton and Tecton in  $\rho/V_p$  and  $\rho/V_s$  would be enlarged if the temperature increase caused by the metasomatism is considered. As shown in Figures 10c and 10d, the  $\rho/V_p$  of the Proton and Tecton SCLM (1500 K) is 1.6%–1.8% and 1.7%–2.1% higher than that of the Archon (1300 K), respectively; and the  $\rho/V_s$  of the Archon (1300 K) is  $\sim 2.2\%$  and  $\sim 2.6\%$  lower than the  $\rho/V_s$  of the Proton and Tecton SCLM (1500 K), respectively. Therefore, in comparison with  $V_p$  and  $V_s$ ,  $\rho/V_p$  and  $\rho/V_s$  are better indicators of chemical variations from the Archon to the Proton and Tecton.

## 5. Conclusions

Single-crystal elastic properties of SCLM Cr-pyrope were measured at high  $P$  and high  $T$  using the BLS method. The obtained elastic parameters were used to examine whether the elastic properties of SCLM Cr-pyrope at the SCLM  $P$ - $T$  conditions can be accurately calculated from those of end-member garnets (end-member model). The results indicate that the end-member model provides a sufficient approximation for the elastic properties of Cr-pyrope in calculating the elastic properties of the SCLM peridotite. The densities and velocities of the Archon, Proton and Tecton are modeled, indicating that the chemical evolution of the SCLM from the Archon to the Tecton significantly increases the density of the SCLM. On the contrary, the chemical evolution does not significantly influence the velocities ( $V_p$  and  $V_s$ ) of the SCLM. By comparison,  $\rho/V_p$  and  $\rho/V_s$  are more sensitive to the chemical variations of the SCLM.

## Conflict of Interest

The authors declare no conflicts of interest relevant to this study.

## Data Availability Statement

Per AGU's Data Policy, the supporting data have been deposited in a general repository, Zenodo, <https://doi.org/10.5281/zenodo.6970424>.



## Acknowledgments

This project was funded by the National Natural Science Foundation of China (41802043), the Youth Innovation Promotion Association CAS (Dawei Fan, 2018434), the Science and Technology Foundation of Guizhou Province (QKHJC-ZK[2021]ZD042), Guangzhong Yang acknowledges the financial support from “The geological research project of Guizhou province—The research of the placer anomaly and mineralogical characteristics of pyrope in Xiawengshao area, Shibing County (2016-02).” The experiments were performed at GeoSoilEnviroCARS (13-BM-D), Advanced Photon Source (APS), and Argonne National Laboratory. The use of gas-loading system is supported by COMPRES and GeoSoilEnviroCARS. GeoSoilEnviroCARS is supported by the National Science Foundation—Earth Sciences (EAR-1634415) and the Department of Energy—Geosciences (DE-FG02-94ER14466). COMPRES is under NSF Cooperative Agreement EAR-1661511. Use of the Advanced Photon Source was supported by the U.S. Department of Energy, Office of Science, Office of Basic Energy Sciences, under Contract No. DE-AC02-06CH11357. We thank the editor for handling this manuscript, and the associate editor and two reviewers for constructive suggestions and comments which helped to improve the manuscript.

## References

- Afonso, J. C., Ranalli, G., Fernández, M., Griffin, W. L., O'Reilly, S. Y., & Faul, U. (2010). On the Vp/Vs–Mg# correlation in mantle peridotites: Implications for the identification of thermal and compositional anomalies in the upper mantle. *Earth and Planetary Science Letters*, 289(3–4), 606–618. <https://doi.org/10.1016/j.epsl.2009.12.005>
- Agashev, A. M., Ionov, D. A., Pokhilenko, N. P., Golovin, A. V., Cherepanova, Y., & Sharygin, I. S. (2013). Metasomatism in lithospheric mantle roots: Constraints from whole-rock and mineral chemical composition of deformed peridotite xenoliths from kimberlite pipe Udachnaya. *Lithos*, 160–161(Supplement C), 201–215. <https://doi.org/10.1016/j.lithos.2012.11.014>
- Angel, R. J., Alvaro, M., & Nestola, F. (2018). 40 years of mineral elasticity: A critical review and a new parameterisation of equations of state for mantle olivines and diamond inclusions. *Physics and Chemistry of Minerals*, 45(2), 95–113. <https://doi.org/10.1007/s00269-017-0900-7>
- Angel, R. J., Gonzalez-Platas, J., & Alvaro, M. (2014). EoSFit7c and a Fortran module (library) for equation of state calculations. *Zeitschrift für Kristallographie - Crystalline Materials*, 229(5), 405–419. <https://doi.org/10.1515/zkri-2013-1711>
- Arimoto, T., Gréaux, S., Irifune, T., Zhou, C., & Higo, Y. (2015). Sound velocities of Fe<sub>3</sub>Al<sub>2</sub>Si<sub>3</sub>O<sub>12</sub> almandine up to 19 GPa and 1700 K. *Physics of the Earth and Planetary Interiors*, 246, 1–8. <https://doi.org/10.1016/j.pepi.2015.06.004>
- Babuška, V., Fiala, J., Kumazawa, M., Ohno, I., & Sumino, Y. (1978). Elastic properties of garnet solid-solution series. *Physics of the Earth and Planetary Interiors*, 16(2), 157–176. [https://doi.org/10.1016/0031-9201\(78\)90086-9](https://doi.org/10.1016/0031-9201(78)90086-9)
- Bass, J. D. (1986). Elasticity of uvarovite and andradite garnets. *Journal of Geophysical Research*, 91(B7), 7505–7516. <https://doi.org/10.1029/JB091iB07p07505>
- Bass, J. D. (1989). Elasticity of grossular and spessartite garnets by Brillouin spectroscopy. *Journal of Geophysical Research*, 94(B6), 7621–7628. <https://doi.org/10.1029/JB094iB06p07621>
- Beyer, C., Kurnosov, A. V., Ballaran, T. B., & Frost, D. J. (2021). High-pressure and high-temperature single-crystal X-ray diffraction of complex garnet solid solutions up to 16 GPa and 823 K. *Physics and Chemistry of Minerals*, 48(4), 17. <https://doi.org/10.1007/s00269-021-01139-5>
- Birch, F. (1947). Finite elastic strain of cubic crystals. *Physical Review*, 71(11), 809–824. <https://doi.org/10.1103/PhysRev.71.809>
- Birch, F. (1978). Finite strain isotherm and velocities for single-crystal and polycrystalline NaCl at high pressures and 300 K. *Journal of Geophysical Research*, 83(B3), 1257–1268. <https://doi.org/10.1029/JB083iB03p01257>
- Bosenick, A., & Geiger, C. A. (1997). Powder X ray diffraction study of synthetic pyrope-grossular garnets between 20 and 295 K. *Journal of Geophysical Research*, 102(B10), 22649–22657. <https://doi.org/10.1029/97JB01612>
- Cameron, M., Sueno, S., Prewitt, C. T., & Papike, J. J. (1973). High-temperature crystal chemistry of acmite, diopside, hedenbergite, jadeite, spodumene, and ureyite. *American Mineralogist*, 58, 594–618.
- Chai, M., Brown, J. M., & Slutsky, L. J. (1997). The elastic constants of a pyrope-grossular-almandine garnet to 20 GPa. *Geophysical Research Letters*, 24(5), 523–526. <https://doi.org/10.1029/97GL00371>
- Chantel, J., Manthilake, G. M., Frost, D. J., Beyer, C., Ballaran, T. B., Jing, Z., & Wang, Y. (2016). Elastic wave velocities in polycrystalline Mg<sub>3</sub>Al<sub>2</sub>Si<sub>3</sub>O<sub>12</sub>-pyrope garnet to 24 GPa and 1300 K. *American Mineralogist*, 101(4), 991–997. <https://doi.org/10.2138/am-2016-5335>
- Chen, G., Cooke, J. A., Gwanmesia, G. D., & Liebermann, R. C. (1999). Elastic wave velocities of Mg<sub>3</sub>Al<sub>2</sub>Si<sub>3</sub>O<sub>12</sub>-pyrope garnet to 10 GPa. *American Mineralogist*, 84(3), 384–388. <https://doi.org/10.2138/am-1999-0322>
- Connolly, J. A. D. (2005). Computation of phase equilibria by linear programming: A tool for geodynamic modeling and its application to subduction zone decarbonation. *Earth and Planetary Science Letters*, 236(1), 524–541. <https://doi.org/10.1016/j.epsl.2005.04.033>
- Deen, T. J., Griffin, W., Begg, G., O'Reilly, S. Y., Natapov, L., & Hronsky, J. (2006). Thermal and compositional structure of the subcontinental lithospheric mantle: Derivation from shear wave seismic tomography. *Geochemistry, Geophysics, Geosystems*, 7(7), Q07003. <https://doi.org/10.1029/2005GC001120>
- Dera, P., Zhuravlev, K., Prakupenka, V., Rivers, M. L., Finkelstein, G. J., Grubor-Urošević, O., et al. (2013). High pressure single-crystal micro X-ray diffraction analysis with GSE\_ADA/RSV software. *High Pressure Research*, 33(3), 466–484. <https://doi.org/10.1080/08957959.2013.806504>
- Deschamps, F., Trampert, J., & Snieder, R. (2002). Anomalies of temperature and iron in the uppermost mantle inferred from gravity data and tomographic models. *Physics of the Earth and Planetary Interiors*, 129(3), 245–264. [https://doi.org/10.1016/S0031-9201\(01\)00294-1](https://doi.org/10.1016/S0031-9201(01)00294-1)
- Djomeni, Y. H. P., O'Reilly, S. Y., Griffin, W., & Morgan, P. (2001). The density structure of subcontinental lithosphere through time. *Earth and Planetary Science Letters*, 184(3–4), 605–621. [https://doi.org/10.1016/S0012-821X\(00\)00362-9](https://doi.org/10.1016/S0012-821X(00)00362-9)
- Du, W., Clark, S. M., & Walker, D. (2015). Thermo-compression of pyrope-grossular garnet solid solutions: Non-linear compositional dependence. *American Mineralogist*, 100(1), 215–222. <https://doi.org/10.2138/am-2015-4752>
- Du, W., Clark, S. M., & Walker, D. (2016). Excess mixing volume, microstrain, and stability of pyrope-grossular garnets. *American Mineralogist*, 101(1), 193–204. <https://doi.org/10.2138/am-2016-5128>
- Duffy, T. S. (2018). Single-crystal elastic properties of minerals and related materials with cubic symmetry. *American Mineralogist*, 103(6), 977–988. <https://doi.org/10.2138/am-2018-6285>
- Dymshits, A. M., Litasov, K. D., Sharygin, I. S., Shatskiy, A., Ohtani, E., Suzuki, A., & Funakoshi, K. (2014). Thermal equation of state of majoritic khorringite and its significance for continental upper mantle. *Journal of Geophysical Research*, 119(11), 8034–8046. <https://doi.org/10.1002/2014JB011194>
- Every, A. (1980). General closed-form expressions for acoustic waves in elastically anisotropic solids. *Physical Review B*, 22(4), 1746–1760. <https://doi.org/10.1103/PhysRevB.22.1746>
- Faccincani, L., Faccini, B., Casetta, F., Mazzucchelli, M., Nestola, F., & Coltorti, M. (2021). EoS of mantle minerals coupled with composition and thermal state of the lithosphere: Inferring the density structure of peridotitic systems. *Lithos*, 404–405, 106483. <https://doi.org/10.1016/j.lithos.2021.106483>
- Fan, D., Fu, S., Lu, C., Xu, J., Zhang, Y., Tkachev, S. N., et al. (2020). Elasticity of single-crystal Fe-enriched diopside at high-pressure conditions: Implications for the origin of upper mantle low-velocity zones. *American Mineralogist: Journal of Earth and Planetary Materials*, 105(3), 363–374. <https://doi.org/10.2138/am-2020-7075>
- Fan, D., Kuang, Y., Xu, J., Li, B., Zhou, W., & Xie, H. (2017). Thermoelastic properties of grossular-andradite solid solution at high pressures and temperatures. *Physics and Chemistry of Minerals*, 44(2), 137–147. <https://doi.org/10.1007/s00269-016-0843-4>
- Fan, D., Xu, J., Lu, C., Tkachev, S. N., Li, B., Ye, Z., et al. (2019). Elasticity of single-crystal low water content hydrous pyrope at high-pressure and high-temperature conditions. *American Mineralogist*, 104(7), 1022–1031. <https://doi.org/10.2138/am-2019-6897>
- Fan, D., Xu, J., Ma, M., Liu, J., & Xie, H. (2015). P-V-T equation of state of spessartine-almandine solid solution measured using a diamond anvil cell and in situ synchrotron X-ray diffraction. *Physics and Chemistry of Minerals*, 42(1), 63–72. <https://doi.org/10.1007/s00269-014-0700-2>

- Fan, D., Xu, J., Ma, M., Wei, S., Zhang, B., Liu, J., & Xie, H. (2015). *P-V-T* equation of state of  $\text{Ca}_3\text{Cr}_2\text{Si}_3\text{O}_{12}$  uvarovite garnet by using a diamond-anvil cell and in-situ synchrotron X-ray diffraction. *American Mineralogist*, *100*(2–3), 588–597. <https://doi.org/10.2138/am-2015-5002>
- Forte, A. M., & Perry, H. C. (2000). Geodynamic evidence for a chemically depleted continental tectosphere. *Science*, *290*(5498), 1940–1944. <https://doi.org/10.1126/science.290.5498.1940>
- Fouch, M. J., James, D. E., VanDecar, J. C., Van der Lee, S., & Group, K. S. (2004). Mantle seismic structure beneath the Kaapvaal and Zimbabwe cratons. *South African Journal of Geology*, *107*(1–2), 33–44. <https://doi.org/10.2113/107.1-2.33>
- Ganguly, J., Cheng, W., & O'Neill, H. S. C. (1993). Syntheses, volume, and structural changes of garnets in the pyrope-grossular join: Implications for stability and mixing properties. *American Mineralogist*, *78*(5–6), 583–593.
- Gréaux, S., & Yamada, A. (2019). Density variations of Cr-rich garnets in the upper mantle inferred from the elasticity of uvarovite garnet. *Comptes Rendus Geoscience*, *351*(2), 95–103. <https://doi.org/10.1016/j.crte.2018.09.012>
- Griffin, W., Fisher, N., Friedman, J., Ryan, C., & O'Reilly, S. (1999). Cr-pyrope garnets in the lithospheric mantle. I. Compositional systematics and relations to tectonic setting. *Journal of Petrology*, *40*(5), 679–704. <https://doi.org/10.1093/ptro/40.5.679>
- Griffin, W., O'Reilly, S., Abe, N., Aulbach, S., Davies, R., Pearson, N., et al. (2003). The origin and evolution of Archean lithospheric mantle. *Precambrian Research*, *127*(1–3), 19–41. [https://doi.org/10.1016/S0301-9268\(03\)00180-3](https://doi.org/10.1016/S0301-9268(03)00180-3)
- Griffin, W., O'Reilly, S. Y., Afonso, J. C., & Begg, G. (2009). The composition and evolution of lithospheric mantle: A re-evaluation and its tectonic implications. *Journal of Petrology*, *50*(7), 1185–1204. <https://doi.org/10.1093/ptrology/egn033>
- Gwanmesia, G., Jackson, I., & Liebermann, R. (2007). In search of the mixed derivative  $\partial^2 M/\partial P \partial T$  ( $M = G, K$ ): Joint analysis of ultrasonic data for polycrystalline pyrope from gas-and solid-medium apparatus. *Physics and Chemistry of Minerals*, *34*(2), 85–93. <https://doi.org/10.1007/s00269-006-0130-x>
- Gwanmesia, G. D., Wang, L., Heady, A., & Liebermann, R. C. (2014). Elasticity and sound velocities of polycrystalline grossular garnet ( $\text{Ca}_3\text{Al}_2\text{Si}_3\text{O}_{12}$ ) at simultaneous high pressures and high temperatures. *Physics of the Earth and Planetary Interiors*, *228*, 80–87. <https://doi.org/10.1016/j.pepi.2013.09.010>
- Gwanmesia, G. D., Zhang, J., Darling, K., Kung, J., Li, B., Wang, L., et al. (2006). Elasticity of polycrystalline pyrope ( $\text{Mg}_3\text{Al}_2\text{Si}_3\text{O}_{12}$ ) to 9 GPa and 1000°C. *Physics of the Earth and Planetary Interiors*, *155*(3), 179–190. <https://doi.org/10.1016/j.pepi.2005.10.008>
- Hao, M., Zhang, J. S., Pierotti, C. E., Zhou, W.-Y., Zhang, D., & Dera, P. (2020). The seismically fastest chemical heterogeneity in the Earth's deep upper mantle—Implications from the single-crystal thermoelastic properties of jadeite. *Earth and Planetary Science Letters*, *543*, 116345. <https://doi.org/10.1016/j.epsl.2020.116345>
- Hill, R. (1952). The elastic behaviour of a crystalline aggregate. *Proceedings of the Physical Society Section A*, *65*(5), 349–354. <https://doi.org/10.1088/0370-1298/65/5/307>
- Holland, T. J. B., Green, E. C. R., & Powell, R. (2018). Melting of peridotites through to granites: A simple thermodynamic model in the system KNCFMASH+Tc. *Journal of Petrology*, *59*(5), 881–900. <https://doi.org/10.1093/ptrology/egy048>
- Holland, T. J. B., & Powell, R. (2011). An improved and extended internally consistent thermodynamic dataset for phases of petrological interest, involving a new equation of state for solids. *Journal of Metamorphic Geology*, *29*(3), 333–383. <https://doi.org/10.1111/j.1525-1314.2010.00923.x>
- Huang, S., & Chen, J. H. (2014). Equation of state of pyrope-almandine solid solution measured using a diamond anvil cell and in situ synchrotron X-ray diffraction. *Physics of the Earth and Planetary Interiors*, *228*, 88–91. <https://doi.org/10.1016/j.pepi.2014.01.014>
- Hugh-Jones, D. (1997). Thermal expansion of  $\text{MgSiO}_3$  and  $\text{FeSiO}_3$  ortho- and clinopyroxenes. *American Mineralogist*, *82*(7–8), 689–696. <https://doi.org/10.2138/am-1997-7-806>
- Ionov, D. A., Doucet, L. S., & Ashchepkov, I. V. (2010). Composition of the lithospheric mantle in the Siberian craton: New constraints from fresh peridotites in the Udachnaya-East kimberlite. *Journal of Petrology*, *51*(11), 2177–2210. <https://doi.org/10.1093/ptrology/eqq053>
- Isaak, D. G., Anderson, O. L., & Oda, H. (1992). High-temperature thermal expansion and elasticity of calcium-rich garnets. *Physics and Chemistry of Minerals*, *19*(2), 106–120. <https://doi.org/10.1007/BF00198608>
- Ita, J., & Stixrude, L. (1992). Petrology, elasticity, and composition of the mantle transition zone. *Journal of Geophysical Research*, *97*(B5), 6849–6866. <https://doi.org/10.1029/92JB00068>
- Jackson, J. M., Sinogeikin, S. V., & Bass, J. D. (2007). Sound velocities and single-crystal elasticity of orthoenstatite to 1073 K at ambient pressure. *Physics of the Earth and Planetary Interiors*, *161*(1–2), 1–12. <https://doi.org/10.1016/j.pepi.2006.11.002>
- Jacobsen, S. D., Liu, Z., Ballaran, T. B., Littlefield, E. F., Ehm, L., & Hemley, R. J. (2010). Effect of  $\text{H}_2\text{O}$  on upper mantle phase transitions in  $\text{MgSiO}_3$ : Is the depth of the seismic X-discontinuity an indicator of mantle water content? *Physics of the Earth and Planetary Interiors*, *183*(1), 234–244. <https://doi.org/10.1016/j.pepi.2010.06.015>
- Jeanloz, R., & Thompson, A. B. (1983). Phase transitions and mantle discontinuities. *Reviews of Geophysics*, *21*(1), 51–74. <https://doi.org/10.1029/RG021i001p00051>
- Klemme, S., Van Miltenburg, J., Javorsky, P., & Wastin, F. (2005). Thermodynamic properties of uvarovite garnet ( $\text{Ca}_3\text{Cr}_2\text{Si}_3\text{O}_{12}$ ). *American Mineralogist*, *90*(4), 663–666. <https://doi.org/10.2138/am.2005.1812>
- Kroll, H., Kirfel, A., Heinemann, R., & Barbier, B. (2012). Volume thermal expansion and related thermophysical parameters in the Mg, Fe olivine solid-solution series. *European Journal of Mineralogy*, *24*(6), 935–956. <https://doi.org/10.1127/0935-1221/2012/0024-2235>
- Leitner, B. J., Weidner, D. J., & Liebermann, R. C. (1980). Elasticity of single crystal pyrope and implications for garnet solid solution series. *Physics of the Earth and Planetary Interiors*, *22*(2), 111–121. [https://doi.org/10.1016/0031-9201\(80\)90052-7](https://doi.org/10.1016/0031-9201(80)90052-7)
- Li, B., & Neuville, D. R. (2010). Elasticity of diopside to 8 GPa and 1073 K and implications for the upper mantle. *Physics of the Earth and Planetary Interiors*, *183*(3), 398–403. <https://doi.org/10.1016/j.pepi.2010.08.009>
- Li, C., van der Hilst, R. D., Engdahl, E. R., & Burdick, S. (2008). A new global model for *P* wave speed variations in Earth's mantle. *Geochemistry, Geophysics, Geosystems*, *9*(5), Q05018. <https://doi.org/10.1029/2007gc001806>
- Lu, C., Mao, Z., Lin, J.-F., Zhuravlev, K. K., Tkachev, S. N., & Prakashenka, V. B. (2013). Elasticity of single-crystal iron-bearing pyrope up to 20 GPa and 750 K. *Earth and Planetary Science Letters*, *361*, 134–142. <https://doi.org/10.1016/j.epsl.2012.11.041>
- Ma, C., Simon, S. B., Rossman, G. R., & Grossman, L. (2009). End-member calcium Tschermak's pyroxene,  $\text{CaAlAlSiO}_6$ , from the Allende and Murray meteorites: Occurrence, origin and significance.
- Malkovets, V., Griffin, W., O'Reilly, S., & Wood, B. (2007). Diamond, subcalcic garnet, and mantle metasomatism: Kimberlite sampling patterns define the link. *Geology*, *35*(4), 339–342. <https://doi.org/10.1130/g23092a.1>
- Mao, H., Xu, J.-A., & Bell, P. (1986). Calibration of the ruby pressure gauge to 800 kbar under quasi-hydrostatic conditions. *Journal of Geophysical Research*, *91*(B5), 4673–4676. <https://doi.org/10.1029/JB091iB05p04673>
- Mao, Z., Fan, D. W., Lin, J. F., Yang, J., Tkachev, S. N., Zhuravlev, K., & Prakashenka, V. B. (2015). Elasticity of single-crystal olivine at high pressures and temperatures. *Earth and Planetary Science Letters*, *426*, 204–215. <https://doi.org/10.1016/j.epsl.2015.06.045>

- Milani, S., Angel, R. J., Scandolo, L., Mazzucchelli, M. L., Ballaran, T. B., Klemme, S., et al. (2017). Thermo-elastic behavior of grossular garnet at high pressures and temperatures. *American Mineralogist*, 102(4), 851–859. <https://doi.org/10.2138/am-2017-5855>
- Milani, S., Nestola, F., Alvaro, M., Pasqual, D., Mazzucchelli, M. L., Domeneghetti, M. C., & Geiger, C. (2015). Diamond–garnet geobarometry: The role of garnet compressibility and expansivity. *Lithos*, 227, 140–147. <https://doi.org/10.1016/j.lithos.2015.03.017>
- Ohashi, Y. (1984). Polysynthetically-twinned structures of enstatite and wollastonite. *Physics and Chemistry of Minerals*, 10(5), 217–229. <https://doi.org/10.1007/BF00309314>
- O'Neill, B., Bass, J. D., Rossman, G. R., Geiger, C. A., & Langer, K. (1991). Elastic properties of pyrope. *Physics and Chemistry of Minerals*, 17(7), 617–621. <https://doi.org/10.1007/BF00203841>
- O'Neill, B., Bass, J. D., Smyth, J. R., & Vaughan, M. T. (1989). Elasticity of a grossular-pyrope-almandine garnet. *Journal of Geophysical Research*, 94(B12), 17819–17824. <https://doi.org/10.1029/JB094iB12p17819>
- Rivers, M., Prakapenka, V. B., Kubo, A., Pullins, C., Holl, C. M., & Jacobsen, S. D. (2008). The COMPRES/GSECARS gas-loading system for diamond anvil cells at the Advanced Photon Source. *High Pressure Research*, 28(3), 273–292. <https://doi.org/10.1080/08957950802333593>
- Sang, L., & Bass, J. D. (2014). Single-crystal elasticity of diopside to 14 GPa by Brillouin scattering. *Physics of the Earth and Planetary Interiors*, 228, 75–79. <https://doi.org/10.1016/j.pepi.2013.12.011>
- Shchukina, E. V., Agashev, A. M., Kostrovitsky, S. I., & Pokhilenko, N. P. (2015). Metasomatic processes in the lithospheric mantle beneath the V. Grib kimberlite pipe (Arkhangelsk diamondiferous province, Russia). *Russian Geology and Geophysics*, 56(12), 1701–1716. <https://doi.org/10.1016/j.rgg.2015.11.004>
- Shu, Q., & Brey, G. P. (2015). Ancient mantle metasomatism recorded in subcalcic garnet xenocrysts: Temporal links between mantle metasomatism, diamond growth and crustal tectonomagmatism. *Earth and Planetary Science Letters*, 418(Supplement C), 27–39. <https://doi.org/10.1016/j.epsl.2015.02.038>
- Shu, Q., Brey, G. P., Gerdes, A., & Hofer, H. E. (2013). Geochronological and geochemical constraints on the formation and evolution of the mantle underneath the Kaapvaal craton: Lu–Hf and Sm–Nd systematics of subcalcic garnets from highly depleted peridotites. *Geochimica et Cosmochimica Acta*, 113(Supplement C), 1–20. <https://doi.org/10.1016/j.gca.2013.03.010>
- Sinogeikin, S. V., & Bass, J. D. (2000). Single-crystal elasticity of pyrope and MgO to 20 GPa by Brillouin scattering in the diamond cell. *Physics of the Earth and Planetary Interiors*, 120(1), 43–62. [https://doi.org/10.1016/S0031-9201\(00\)00143-6](https://doi.org/10.1016/S0031-9201(00)00143-6)
- Sinogeikin, S. V., & Bass, J. D. (2002). Elasticity of pyrope and majorite–pyrope solid solutions to high temperatures. *Earth and Planetary Science Letters*, 203(1), 549–555. [https://doi.org/10.1016/S0012-821X\(02\)00851-8](https://doi.org/10.1016/S0012-821X(02)00851-8)
- Soga, N. (1967). Elastic constants of garnet under pressure and temperature. *Journal of Geophysical Research*, 72(16), 4227–4234. <https://doi.org/10.1029/JZ072i016p04227>
- Suzuki, I., & Anderson, O. L. (1983). Elasticity and thermal expansion of a natural garnet up to 1000 K. *Journal of Physics of the Earth*, 31(2), 125–138. <https://doi.org/10.4294/jpe.1952.31.125>
- Tribaudino, M., Nestola, F., Bruno, M., Ballaran, T. B., & Liebske, C. (2008). Thermal expansion along the NaAlSi<sub>2</sub>O<sub>6</sub>-NaFe<sup>3+</sup>Si<sub>2</sub>O<sub>6</sub> and NaAl-Si<sub>2</sub>O<sub>6</sub>-CaFe<sup>2+</sup>Si<sub>2</sub>O<sub>6</sub> solid solutions. *Physics and Chemistry of Minerals*, 35(5), 241–248. <https://doi.org/10.1007/s00269-008-0217-7>
- Wang, Z., & Ji, S. (2001). Elasticity of six polycrystalline silicate garnets at pressure up to 3.0 GPa. *American Mineralogist*, 86(10), 1209–1218. <https://doi.org/10.2138/am-2001-1009>
- Wei, W., Mao, Z., Sun, N., Sun, D., & Tkachev, S. N. (2021). High pressure-temperature single-crystal elasticity of grossular: Implications for the low-velocity layer in the bottom transition zone. *Geophysical Research Letters*, 48(9), e2021GL093540. <https://doi.org/10.1029/2021gl093540>
- Wu, F.-Y., Yang, J.-H., Xu, Y.-G., Wilde, S. A., & Walker, R. J. (2019). Destruction of the North China craton in the Mesozoic. *Annual Review of Earth and Planetary Sciences*, 47(1), 173–195. <https://doi.org/10.1146/annurev-earth-053018-060342>
- Xu, J., Fan, D., Zhang, D., Guo, X., Zhou, W., & Dera, P. K. (2020). Phase transition of enstatite-ferrosilite solid solutions at high pressure and high temperature: Constraints on metastable orthopyroxene in cold subduction. *Geophysical Research Letters*, 47(12), e2020GL087363. <https://doi.org/10.1029/2020GL087363>
- Xu, J., Fan, D., Zhang, D., Ma, M., Zhou, Y., Tkachev, S. N., et al. (2022). Phase transitions of Fe-Al- and Ca-bearing orthopyroxenes at high pressure and high temperature: Implications for metastable orthopyroxenes in stagnant slabs. *Journal of Geophysical Research: Solid Earth*, 127(1), e2021JB023133. <https://doi.org/10.1029/2021JB023133>
- Xu, J., Zhang, D., Fan, D., Dera, P. K., Shi, F., & Zhou, W. (2019). Thermoelastic properties of eclogitic garnets and omphacites: Implications for deep subduction of oceanic crust and density anomalies in the upper mantle. *Geophysical Research Letters*, 46(1), 179–188. <https://doi.org/10.1029/2018GL081170>
- Xu, J., Zhang, D., Fan, D., Zhang, J. S., Hu, Y., Guo, X., et al. (2018). Phase transitions in orthoenstatite and subduction zone dynamics: Effects of water and transition metal ions. *Journal of Geophysical Research: Solid Earth*, 123(4), 2723–2737. <https://doi.org/10.1002/2017JB015169>
- Yang, H., & Ghose, S. (1994). Thermal expansion, Debye temperature and Grüneisen parameter of synthetic (Fe, Mg)SiO<sub>3</sub> orthopyroxenes. *Physics and Chemistry of Minerals*, 20(8), 575–586. <https://doi.org/10.1007/BF00211853>
- Zhang, J. S., & Bass, J. D. (2016a). Single crystal elasticity of natural Fe-bearing orthoenstatite across a high-pressure phase transition. *Geophysical Research Letters*, 43(16), 8473–8481. <https://doi.org/10.1002/2016GL069963>
- Zhang, J. S., & Bass, J. D. (2016b). Sound velocities of olivine at high pressures and temperatures and the composition of Earth's upper mantle. *Geophysical Research Letters*, 43(18), 9611–9618. <https://doi.org/10.1002/2016GL069949>
- Zhang, L., Ahsbahs, H., & Kutoglu, A. (1998). Hydrostatic compression and crystal structure of pyrope to 33 GPa. *Physics and Chemistry of Minerals*, 25(4), 301–307. <https://doi.org/10.1007/s002690050118>
- Zhao, Y., Dreele, R. V., Zhang, J., & Weidner, D. (1998). Thermoelastic equation of state of monoclinic pyroxene: CaMgSi<sub>2</sub>O<sub>6</sub> diopside. *The Review of High Pressure Science and Technology*, 7, 25–27. <https://doi.org/10.4131/jshpreview.7.25>
- Zhao, Y., Von Dreele, R. B., Shankland, T. J., Weidner, D. J., Zhang, J., Wang, Y., & Gasparik, T. (1997). Thermoelastic equation of state of jadeite NaAlSi<sub>3</sub>O<sub>6</sub>: An energy-dispersive Reitveld Refinement Study of low symmetry and multiple phases diffraction. *Geophysical Research Letters*, 24(1), 5–8. <https://doi.org/10.1029/96GL03769>
- Zhu, R., Xu, Y., Zhu, G., Zhang, H., Xia, Q., & Zheng, T. (2012). Destruction of the North China craton. *Science China Earth Sciences*, 55(10), 1565–1587. <https://doi.org/10.1007/s11430-012-4516-y>
- Zou, Y., Gréaux, S., Irifune, T., Whitaker, M. L., Shinmei, T., & Higo, Y. (2012). Thermal equation of state of Mg<sub>3</sub>Al<sub>2</sub>Si<sub>3</sub>O<sub>12</sub> pyrope garnet up to 19 GPa and 1700 K. *Physics and Chemistry of Minerals*, 39(7), 589–598. <https://doi.org/10.1007/s00269-012-0514-z>
- Zou, Y., Irifune, T., Gréaux, S., Whitaker, M. L., Shinmei, T., Ohfuji, H., et al. (2012). Elasticity and sound velocities of polycrystalline Mg<sub>3</sub>Al<sub>2</sub>(SiO<sub>4</sub>)<sub>3</sub> garnet up to 20 GPa and 1700 K. *Journal of Applied Physics*, 112(1), 014910. <https://doi.org/10.1063/1.4736407>